Master's thesis

NTNU
Norwegian University of Science and Technology
Faculty of Natural Sciences
Department of Biology

Mikkel Bjerkvoll

Aerial & Underwater Hyperspectral Imagery For Shallow Benthic Nature Type Mapping

Master's thesis in Ocean Resources
Supervisor: Geir Johnsen
Co-supervisor: Torkild Bakken, Aksel A. Mogstad
May 2022

Photomosaic: photos by Asgeir Sørensen & Pål Kvaløy

NTNU
Norwegian University of
Science and Technology

Mikkel Bjerkvoll

Aerial & Underwater Hyperspectral Imagery For Shallow Benthic Nature Type Mapping

Master's thesis in Ocean Resources
Supervisor: Geir Johnsen
Co-supervisor: Torkild Bakken, Aksel A. Mogstad
May 2022

Norwegian University of Science and Technology
Faculty of Natural Sciences
Department of Biology

NTNU
Kunnskap for en bedre verden

Acknowledgement

This thesis was done at Trondhjem Biological Station (TBS), at the dept. of biology, with guidance and assistance from the Norwegian University of Science and Technology (NTNU) as a part of the Seabee research infrastructure project (NFR project number 296478) between January 2021 and May 2022. The field campaigns were done at Sletvik Field Station (NTNU) in Hopavågen, Agdenes. Field campaigns were performed as a part of NTNU Centre for Autonomous Marine Operations and Systems (NTNU AMOS), with help from NTNU dept. of Engineering Cybernetics, dept. of Marine Technology, and dept. of Biology. This degree is based on data collected by teams of researchers from these departments, and would not be possible without the coordination of these researchers.

Big thanks to my main supervisor Geir Johnsen at TBS for introducing me to the world of hyperspectral imagery, and remote sensing. Your guidance sparked my interest for technological application in ecological studies. I've learnt so much from you, and also met a lot of kind, knowledgeable and clever people through you. Your field logistics ultimately enabled this multi-platform thesis.

Aksel Mogstad, you're probably not going to read this but the guidance you've given, the discussions we've had, man you are clever. You deserve a lot of the credit for the ideas of this thesis. Thank you, and good luck at Equinor.

Thank you to Torkild Bakken at NTNU Vitenskapsmuseet. You kept me grounded in ecology and NiN, despite my tendency to get distracted by and fascinated with the technology. I truly appreciate your guidance.

Thanks to Stephen Grant & Rune Bjørgum (NTNU TBS), Kristoffer Gryte & Joseph Garret (Dept. of Engineering Cybernetics, NTNU) along with so many more, for collecting and processing data, and teaching me the ropes. And special thanks to professor Paul Gader (University of Florida) for great discussions for and teaching me about classification and maths.

Lastly, to Marte O. Søreng, Maren Thu, Annecken Nøland, Camilla Marnor and Malin B. Nevstad, thank you so much. It has been great to complete this thesis as part of a team of clever and dedicated students. You have been great discussion partners, and taught me a lot as we have learnt about applied technology together. We are done studying now, but I'm looking forward to seeing you again later, who knows, maybe one of you will be my boss one day.

Trondheim, May 2022

Mikkel Bjerkvoll

Abstract

The Nature in Norway (NiN) system classifies nature types according to environmental variables. Large scale mapping of benthic nature types by water is challenging, as light is quickly attenuated in deep areas and shallow water is difficult to traverse. Existing data of benthic nature types are mainly based on point-measurements. To improve the accuracy and detail of NiN, extensive mapping of the Norwegian coastline is essential.

For the purposes of this study, shallow benthic nature types are classified according to dominant pigment groups. This allows for pigment based classification of hyperspectral photomosaics, and hence relation from image to the nature type system. This study applied an Unmanned Surface Vehicle (USV) and an Unmanned Aerial Vehicle (UAV), both carrying hyperspectral imagers, mapping the same area in Hopavågen, Norway. The class identification potential was described for each photomosaic. The hyperspectral photomosaics were classified using the Spectral Angle Mapper (SAM), and the classification accuracy was assessed for the photomosaics obtained with the USV and UAV.

USV and UAV are promising large scale mapping tools, but it was established that further studies should take place in the spring/summer to obtain sufficient light signal. SAM classification of the USV photomosaic had an accuracy of 63.4%, while the classified UAV photomosaic had an accuracy of 24.8%. Seagrass and brown algae were classified poorly, while red algae and sediment were classified quite well.

Sammendrag

Natur i Norge (NiN) systemet klassifiserer naturtyper basert på miljøvariabler. Storskala kartlegging av bentiske naturtyper er vanskelig, ettersom lys utslukkes fort på dype områder, og grunt vann er vanskelig å forsere. Eksisterende kunnskap om bentiske naturtyper er stort sett basert på punktmålinger. For å forbedre nøyaktigheten og detaljenivået i NiN kreves omfattende kartlegging av norsk kyst.

I denne studien ble bentiske naturtyper klassifisert etter dominerende pigmentgrupper. Denne studien tar i bruk et ubemannet overflatefartøy (USV) og et ubemannet luftfartøy (UAV), begge utstyrt med en hyperspektral bildetaker, og kartlegger det samme området i Hopavågen, Norge. Potensialet for klasseidentifisering blir beskrevet for begge fotomosaikkene. De hyperspektrale fotomosaikkene blir også klassifisert med spektral vinkelkartlegger (SAM), og klassifiseringsnøyaktighet vurderes for fotomosaikkene fra USV og UAV.

UAV og UAV er begge lovende verktøy for storskala kartlegging, men det etableres også at videre studier må gjøres i vår- og sommerhalvåret, for å oppnå bra nok signal. SAM-klassifisering i USV fotomosaikken har en nøyaktighet på 63.4%, og den klassifiserte UAV fotomosaikken har en nøyaktighet på 24.8%. Sjøgress og brunalger ble klassifisert dårlig, mens rødalger og sediment ble klassifisert bra.

Abbreviations & symbols

α	Spectral angle
AMOS	Centre for Autonomous Marine Operations and Systems
BIL	Band Interleaved by Lines
Chl	Chlorophyll
$\mathbf{E_d}(\lambda)$	Downwelling Spectral irradiance (Wm^{-2})
ENVI	Environment for Visualizing Images
FFC	Flat Field Correction
HI	Hyperspectral Imager
IMU	Inertial Measurement Unit
NTNU	Norges Teknisk-Naturvitenskapelige Universitet
NIVA	Norwegian Institute of Water Research
NiN	Natur i Norge
OOI	Object of Interest
RGB	Red, Green and blue
ROI	Region of interest
SAM	Spectral Angle Mapper
SD	Standard Deviation
TBS	Trondhjem Biologiske stasjon, NTNU
UAV	Unmanned Aerial Vehicle
UHI	Underwater Hyperspectral Imager
USV	Unmanned Surface Vehicle
$\mathbf{L_u}(\lambda)$	Upwelling spectral radiance ($Wm^{-2}sr^{-1}$)
IOP	Inherrent Optical Properties
$\mathbf{R}(\lambda)$	Relative spectral reflectance

Contents

Chapter 1

Introduction

The extent of antropogenic effects on coastal environments has increased dramatically in the last century (Halpern et al. 2019, Peirano et al. 2005, Marshall 2021). Coastal seabed mapping is essential in the effort to gain a deeper understanding of these effects, and to increase public awareness of the diversity in the ocean, which in turn may help conservation of oceans species and habitat diversity (de la Torriente et al. 2019, Lieske et al. 2014). There is a current need for systematic habitat mapping and monitoring that is easily conveyed to the public and for an improved management of different taxa and corresponding decision-making (Halvorsen et al. 2015, Cohen et al. 2020).

In the coming years, the SeaBee research infrastructure project (Funded by the Norwegian Research Council) is aiming to create infrastructure for remote sensing of biodiversity in shallow areas along the Norwegian coast (Walday et al. 2021, Rinde et al. 2021). This is an important step in increasing the data base for the marine section of the Nature in Norway system. It is important to assess the functionality of mapping methods that cover large areas efficiently. Such methods should be able to map biodiversity at a high spatial accuracy. Unmanned Aerial Vehicle (UAV) is a quick and efficient mapping tool increasingly making remote sensing a simple tool with a wider range of access (Everaerts et al. 2008, Ventura et al. 2018). Marine mapping is however challenging from a UAV, with only optically shallow areas available (Freitas et al. 2018, Montes-Herrera et al. 2021).

1.1 Nature in Norway - NiN

Nature in Norway (NiN) is a nature type organization system created by Artsdatabanken, together with the University of Oslo (UiO) and Norwegian institute of water research (NIVA). It is intended to set objective and verifiable methods for classifying nature types when mapping flora and fauna in Norway. The system contains three major levels of mapping: Landscape types, nature types, and life medium (Erikstad et al. 2019, Halvorsen et al. 2015, Ødegaard et al. 2009). The three levels are utilized depending on the needs of the end user. This study focuses on the nature type system. It is built hierarchically with main type groups, main types, and basic types.

Nature systems are split into two sub-categories which together aim to completely explain the variations seen in the Norwegian ecosystem. The first category is the type-system, containing the most commonly used nature types (Halvorsen et al. 2015). The second is a complementary description system containing a plethora of secondary environmental variables which ad descriptive complexity to the system (Halvorsen et al. 2015).

1.2 From nature types to pigment based classes

The NiN nature system describes a collection of species living under the same environmental variables as a nature type. With significance of the environmental variables determining the hierarchy of the system. For example within euphotic solid seafloor (main type M1), the types are determined by water influence intensity, i.e. the intensity of currents and wave action, depth related light attenuation, and marine salinity. Which makes up the three most important variables in this environment.

In the NiN system, nature types are organized according to the environmental variables which support the appearance of a selection of species. When mapping classes with a hyperspectral imager (HI), the nature types must be reorganized as pigment-based classes. The pigment composition of a nature type is either decided by the dominant organism group, or the dominant substrate of the nature type. In the case of the main type called Euphotic marine solid bottoms (M1); some subtypes are dominated by Phaeophyta (brown algae), specifically types M1 1-7, and types M1 24-27. The remainder types are dominated by organism groups other than brown algae or exposed substrates. In this case it is beneficial to reorganize the types into a class based on the dominant pigment group; brown algae. The pigments absorb light at different wavelengths, resulting in reflectance of different colors (Johnsen, Leu & Gradinger 2020). Similarly, other nature types must be reorganized according to their dominant pigment group. The following list shows

the nature types and their assigned spectral classes. This reclassification is limited to the optically shallow marine nature types.

- **Seagrass: M7 Marine underwater meadows**
  Main type M7 comprises four types which are differentiated based on depth and salinity. Neither of these parameters are easily inferred from hyperspectral photomosaics, hence the spectral class comprises the whole main type. *Zostera* (Seagrass) contain chlorophyll (chl) *a* and *b* which are the main contributors to the reflectance spectrum giving notable peaks at 550 nm and 630 nm, which is also the lowest absorption. (Ralph et al. 2002, Casazza & Mazzella 2002).

- **Red algae: M1 Euphotic marine solid bottoms (type 2) & M4 Euphotic marine sediment bottoms (type 11-20)**
  Rhodophyta describes both leafy red algae, and Corallinales (coralline algae), which due to the calciferous structure of coralline algae, have a slightly different R(λ) (Hochberg & Atkinson 2003, Johnsen, Leu & Gradinger 2020). This study uses the term "red algae" for nature types which are dominated by coralline algae, but may also contain other forms of Rhodophyta. Arrangement of sediment grain size is the main environmental variable differentiating within M4. Calciferous red algae require a certain grain size as reliable substrates, hence only a handful of the M4 types are organized as red algae. Chl *a* and R-phycoerythrin are the prominent contributors to the *in vivo* reflectance spectrum of coralline algae (Mogstad & Johnsen 2017).

- **Brown algae: M1 Euphotic marine solid bottoms (type 3-7 & 24-27) & M3 Solid intertidal bottoms (type 1-7)**
  The previously mentioned environmental variables differentiate between M1 types. Types within M3 are differentiated by water influence intensity, air exposure time and salinity. The brown algae class comprises the types within M1 and M3 dominated brown algae, which are of high salinity, not too deep, and not too steep. Chl *a*, chl *c* and fucoxanthin are the dominant contributors to the reflectance spectrum of brown algae (Colombo-Pallotta et al. 2006, Johnsen, Leu & Gradinger 2020).

- **Sediment: M1 Euphotic marine solid bottoms (type 7-14) & M4 Euphotic marine sediment bottoms (type 1-12)**
  Water with lower than usual salt content (brackish) and most extremes of other environmental variables often leave sediments exposed, as sessile organisms struggle to settle. The distinctiveness of the sediment is its lack of pigmentation, resulting in a generally featureless optical fingerprints. Hence, this spectral class comprises a wide variety of nature types.

1.3 Remote sensing

Remote sensing is defined as the non intrusive gathering of information at a distance, but more commonly refers to the use of an optical sensor utilizing several regions of the electromagnetic spectrum (Campbell & Wynne 2011). Usually, remote sensing data has been gathered from satellites, but also from platforms closer to the object of interest (OOI) (figure 1.1). Recent advances in techonolgy has allowed for the use of light weight UAVs for remote sensing (Kislik et al. 2018). A UAV is a good tool for remote sensing of the seafloor, with no upper limit to where in the water column it can observe, and without disturbing the sediment (Kutser et al. 2006). It is however limited to only optically shallow waters, by the depth and attenuation of the water column. An HI mounted on a UAV is a passive sensor, relying on sunlight to obtain signal (Johnsen, Mogstad, Berge & Cohen 2020).

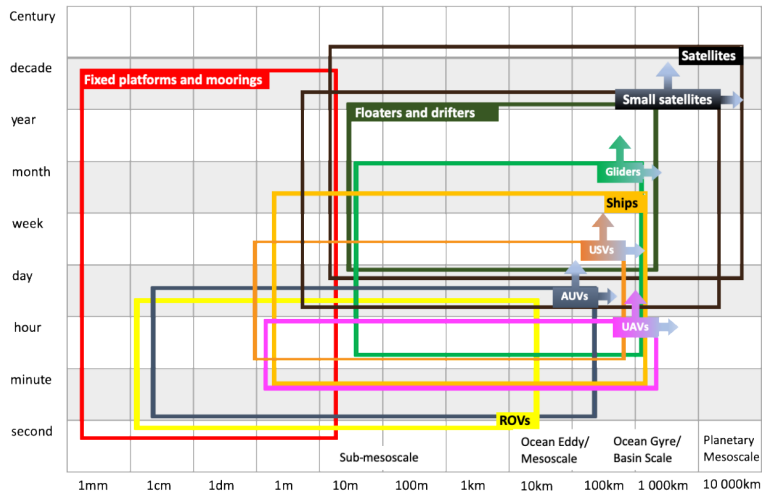

Figure 1.1: Platforms used in remote sensing primarily differ in their temporal and spatial scale. Remotely operated vehicle (ROV), Autonomous underwater vehicle (AUV), Unmanned surface vehicle (USV) and Unmanned aerial vehicles (UAV) are the most common for shallow benthic surveys. From (Sørensen et al. 2020).

1.4 Hyperspectral imaging and Optical fingerprints

A hyperspectral imager, also known as imaging spectrometry, is commonly defined as an imager which measures light intensity with a spectral resolution smaller than 10 nm, over a certain interval of wavelengths (Montes-Herrera et al. 2021). The increased spectral resolution reveals several dimensions of color related information which is unavailable for normal cameras and the human eye (figure 1.2).

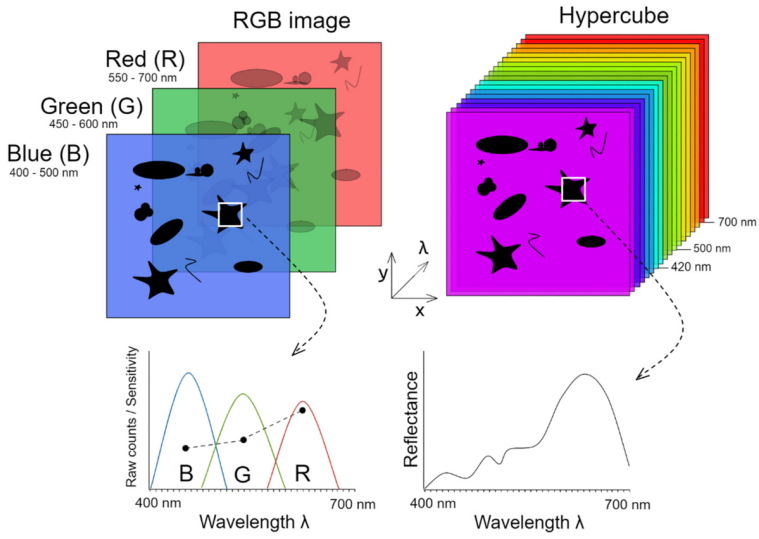

Figure 1.2: The human eye and conventional cameras are only sensitive to light intensity in three wavelength bands: Red, Green and Blue (RGB). A hyperspectral imager is defined as any imager which captures light intensity in continuous bands smaller than 10 nm (Montes-Herrera et al. 2021).

Hyperspectral imagers captures light at intensity ranges decided by their bit-depth. In the raw data, light intensity is stored as a digital count. Imager specific calibrations give the conversion from raw data to radiance upwelling ($L(\lambda)$, $Wm^{-2}sr^{-1}$, Thorne et al. 1997). This study refers to both light absorption, and light reflectance, as a function of wavelengths. Absorption is the inverse of reflectance, hence an absorption peak is the same as a reflectance dip, and visa versa. The imagers used in this study are push broom scanners, which capture a cross track line of pixels simultaniously. The cross track lines will the be stitched together to become a hyperspectral photomosaic (Wolfe 1997, Fajardo 2019).

Water attenuates light strongly, only the upper 100 m receive light in the open oceans, whereas coastal waters are less transparent (Smith & Baker 1978). While containing a higher concentration of constituents, coastal water also contains a larger diversity of constituents, making the attenuation per wavelength very complex. Remote sensing of coastal benthic habitats requires recognition of the water constituents. Inherent optical properties (IOP, comprising phytoplankton, colored dissolved organic matter and total suspended matter) make up the light altering constituents in water. A common method of accounting for the IOPs requires a white reflectance standard in the image. If one assumes that the seafloor is flat and at the same depth as the reflectance standard, this is called a "flat bottom as-

sumption" (Rubasingam et al. 2011). This allows for radiometric correction of IOPs according to equation 1.1 (Mogstad & Johnsen 2017) where $E_d(\lambda)(Wm^{-2})$ is the downwelling spectral irradiance. When investigating processed hyperspectral data, each pixel or object of interest (OOI) reveals a curve displaying light intensity as a function of wavelength, which is the optical fingerprint ($R(\lambda)$). Equation 1.1 gives ($R(\lambda)$), a dimensionless value where the OOI has an intensity value between 0-1 for each wavelength, where 1 is 100% reflectance, and 0 is 0% reflectance. It is important to note that there are are $R(\lambda)$ differences within nature types and species in the pigment based classes. The pigment based classes are a general simplification which aims to capture the most important separators.

$$R(\lambda) = \frac{L_u(\lambda)}{E_d(\lambda)} \tag{1.1}$$

1.5 Spectral mixing

Spectral mixing is a prevailing obstacle to correct classification in most situations (Smith et al. 1990). The $R(\lambda)$ of a pixel contains the reflected light of all objects in that pixel. A combination of different photosynthetic organisms and objects are commonly captured in the same pixel, resulting in a mixing of the spectral reflectance innate to the organisms and objects (Hochberg et al. 2003). Spectral mixing is a common problem in hyperspectral imaging. Spectral unmixing through inverse modelling is hence a common practice in satellite based hyperspectral imaging (Heylen et al. 2014). Higher spatial resolution available with proximate remote sensing platforms (Montes-Herrera et al. 2021), i.e. USV and UAV severely reduces the need for spectral unmixing models.

1.6 Spectral Angle Mapper - SAM

One of the most common classification tools in remote sensing is Spectral Angle Mapper (SAM) (Kutser et al. 2006, Freitas et al. 2018, Rossiter et al. 2020). SAM is a simple method of comparing complex spectral signatures, as n-dimensional vectors, and measuring the angle between these (Kruse et al. 1993). Samples are classified according to how similar they are to a spectrum from the training data set. The training data set contains $R(\lambda)$ of spectral classes. It is often sampled *in vivo* (Mogstad & Johnsen 2017), but can also be sampled during field work (Freitas et al. 2018). All pixels are classified within a user defined parameter called the "spectral angle". The spectral angle is often a heuristically chosen parameter (Freitas et al. 2018), meaning the value is chosen quickly and conveniently, often according to what has worked previously. The spectral angle must be between 0° and 90°. This is because the dimensions of a spectral vector consist of the color

channel which make up the vector, often just three dimensions (RGB). In the case of hyperspectral data, there are hundreds of color channels. The light intensity of any color channel can only be a positive value, so the spectral vectors must be situated in the positive-positive quadrant (if imagining a 2-dimensional space. The equivalent is called the positive hyperoctant in an n-dimensional space). An angle close to 0° means the two spectra are similar (Rashmi et al. 2014).

There are several different methods to assess the accuracy of a classification (Freitas et al. 2018, De Leeuw et al. 2006), but the general concept remains the same. The classified photomosaic is compared with another classified photomosaic. The other photomosaic is for all purposes seen as the "true" classification, unless one is comparing two different classifications. The percentage of pixels which are put to the same class by both methods represent the classification accuracy of the tested method.

1.7 Aim of the study

This study applies two relatively new portable remote sensing platforms to image the same seafloor with imaging spectrometers, from the surface, and from the air. The observed pigment based classes are analyzed in the hyperspectral images from both platforms to describe the quality of class identification in both photomosaics. The photomosaics are then classified using the common SAM classification method (Kruse et al. 1993). The accuracy of both classifications are compared, and both classifications are analyzed and compared to identify advantages and disadvantages of the two platforms. These analyses combine to assess and compare the platforms as methods of nature type mapping.

This study is performed in coordination with Marte O. Søreng (2022). Her study maps a vulnerable shallow habitat, specifically a seagrass meadow, using a USV based UHI. The study discusses and compares other methods of classification, and the potential for USV based mapping of vulnerable habitats. The SAM classification used on the USV photomosaic of this study is comparable to the classifications used in Marte O. Søreng (2022), and her study will be referred to later in this thesis.

Chapter 2

Materials and Methods

September 9th 2021 and March 4th 2022, two parallel surveys were performed. An unmanned surface vehicle (USV) and an unmanned aerial vehicle (UAV) traveled between the same two waypoints, both imaging the seafloor below. The USV carried an underwater hyperspectral imager (UHI), and the UAV carried a hyperspectral imager (HI). This chapter describes the equipment used, mission procedures, as well as processing of the data.

The USV carried a UHI, and the UAV carried a HI. As vehicles travel, transverse lines of pixels are recorded at a given frame rate (Hz, range (UHI: 0.1-90 Hz, HI: 0.1-330 Hz), which are then stitched together to a complete photomosaic. This method of recording is called "push broom scanning" (Fajardo 2019). The along track resolution is dependent on the vehicle speed and frame rate, whereas the cross track resolution is dependent on the distance between the lens and object.

This study compares hyperspectral transect photomosaics captured from two different platforms, the USV and the UAV. These will hereby be described as the USV photomosaic and the UAV photomosaic to avoid confusion.

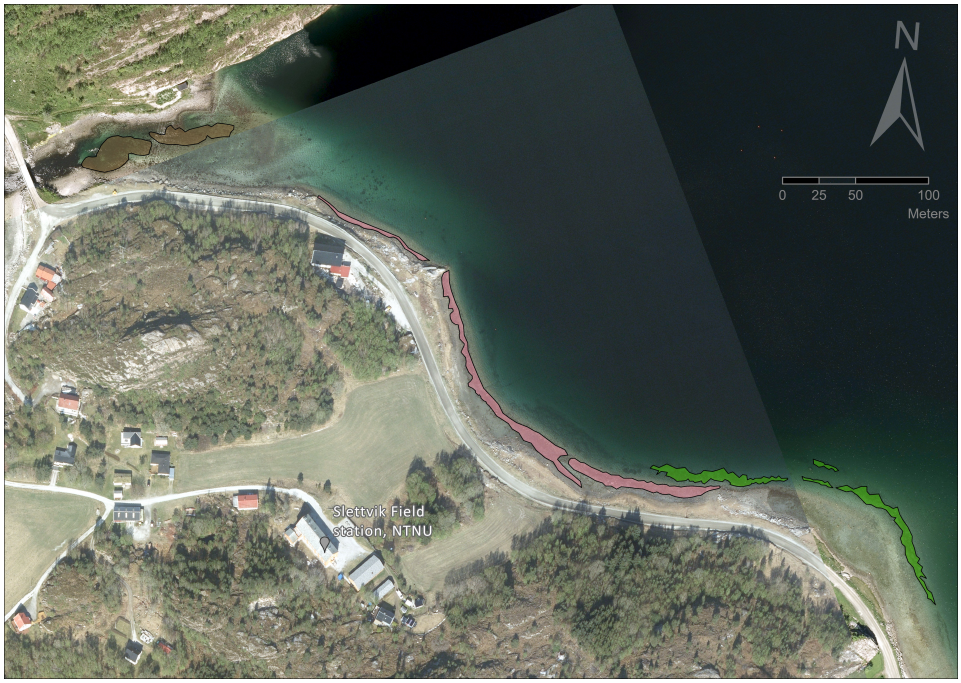

Figure 2.1: Orthophoto of Hopavågen (63°35'N, 9°32'E). Approximate observed extent of dominant classes during field trips in May and September of 2021. Polygons denote Red algae (red), Seagrass (green), and Brown algae (Brown). Colored areas created using the geographical information system (GIS) software ArcGIS (Esri Inc., Redlands, USA) by investigating Ortophoto from Norwegian Mapping Authorities (2019).

2.1 Study Area

Hopavågen (63°35'N, 9°32'E) is a sheltered shallow bay in Agdenes, on the coast of Trøndelag. A narrow stream called "Straumen", in the west end, secures water exchange with Kråkvågfjorden, mainly through tidal action. A few small creeks along the southeastern to northeastern border feed Hopavågen with freshwater regularly. The insignificant in-flowing freshwater has no effect on the biodiversity in the bay (van Marion 1996). The bay only has an estimated exchange rate of 4% to 8% of total volume per day through Straumen, meaning detritus will remain for a long time. The water is also stratified near the bottom of the bay, with a zone of little to no water exchange below 25 meters depth (pers. com. Geir Johnsen & Torkild Bakken, van Marion 1996).

Steep cliffs and bedrock line the northern and north-eastern boundaries of Hopavågen. The southern and western shores consist of fine sediment, with interspersed

rocks in the intertidal zone. The species composition is described as similar to that which is found outside of Straumen, except a notable lack of brown algae in the littoral and sublittoral zone (van Marion 1996). Several species and a high biomass of brown algae was observed in the Straumen area (Figure 2.1). Namely the species *Laminaria hyperborea* (Foslie, 1884), *Alaria esculenta* (Greville, 1830) & *Saccharina latissima* (Linnaeus). Recent studies also describe other species of brown algae in Hopavågen, such as *Fucus serratus* (Linnaeus, 1753), *Colpomenia peregrina* (Hamel, 1937), *Chordaria flagelliformis* (Agardh, 1817) & *Chorda filum* (Stackhouse, 1797, Alvsvåg 2017, Marte O. Søreng 2022). Loose rocks along the southern and western shores are covered in *Corallina officinalis* (Linnaeus 1758), *Phymatolithon* sp. (foslie 1898), & *Lithophyllum orbiculatum* (Foslie 1895)(Red algae, van Marion 1996). Hopavågen also has a seagrass meadow of *Zostera* sp. (Seagrass, further info in Marte O. Søreng 2022) along the middle south shore. The seagrass meadow and the red algae shores as well as parts of Straumen are the areas covered in this study, as these areas cover the pigment based classes (figure 2.1).

Previously acquired samples in Hopavågen include Chlorophyta (green algae) and several invertebrate species (*Strongylocentrotus* sp. (Brandt, 1835), *Echinus esculentus* (Linnaeus, 1758), *Henricia* sp. (Gray, 1840), *Porania pulvillus* (Müller, 1776), *Ceramaster granularis* (Retzia, 1783), *Psolus squamatus* (Müller, 1776), *Stichastrella rosea* (Müller, 1776), *Ophiothrix fragilis* (Müller, 1789) & *Ophiocomina nigra* (Müller, 1789, van Marion 1996). However, no invertebrates appear very dominant in any nature types, and were not expected to be observed from the UAV.

The USV-path runs a line of 48 meters parallel with the shore (figure 2.2), to cover a known seagrass meadow in Hopavågen, with a recorded average depth of 174 cm during the mission period, when the tide was 140 cm above sea map 0 cm. The area covered by the USV is approximately 120 m^2. The first part of the transect is a dense seagrass meadow, dispersed with boulders covered with plumose anemones and red algae. Along the transect the seagrass coverage became less dense, giving way to fine sediment, and more dispersed rocks covered with red algae.

2.2 Physical sampling and *In vivo* spectrometry

Aksel A. Mogstad started a spectral library in 2016, when receieving samples of *Phymatolithon tenue* (Rosenvinge, 1893), and three other red algae (Mogstad & Johnsen 2017). In subsequent studies and courses done at TBS), other species and groups have been recorded, namely species of Chlorophyta, Phaeophyta, Echinodermata, Cnidaria and seagrass. These are the main organism groups observed in Hopavågen. Over the course of two field campaigns in October 2020, May 2021, and September 2021, the spectral library was expanded with more samples of the

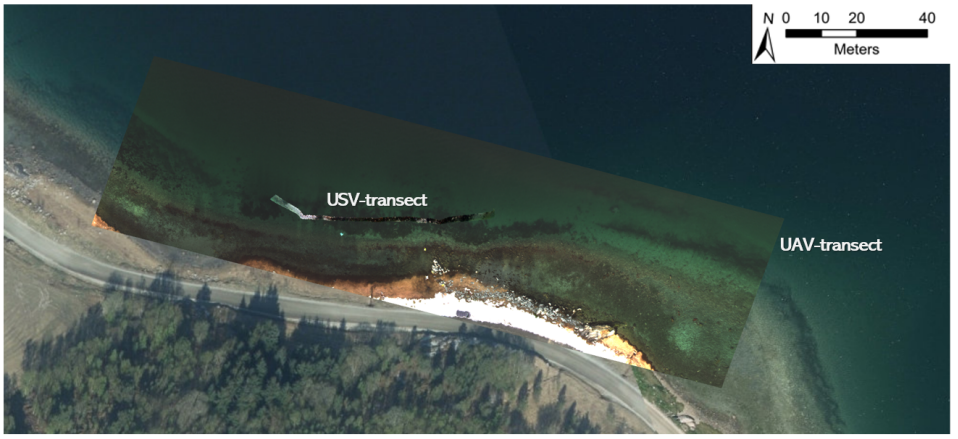

Figure 2.2: The smaller transect line shows the extent of the USV photomosaic covering a line in the seagrass meadow, while the large image is the photomosaic captured in the UAV-transect. Created in ArcGIS. Base map layer from Kartverket (2019)

same groups, also collected from Hopavågen. At the time of this study, the spectral library contains 515 samples.

All samples were analyzed in the lab at NTNU, Sletvik field station, where they were kept in flow through aquariums. The flow through systems continuously provided seawater from a depth of 10 m in Hopavågen. *In vivo* spectrometry was performed as described in Mogstad & Johnsen (2017) using a QE Pro spectrometer (Ocean Optics inc., Largo, USA) connected to a fibre optic cable, illuminated by a halogen light source (HL-2000-HP, Ocean Optics Inc., Largo, USA). It has a spectral resolution of 0.7 nm, covering a range of 347-1113 nm. Several samples collected while snorkelling were added to the spectral library (total n=515). Red algae (n=70), brown algae (n=56), seagrass (n=5) and sediment (n=6) were recorded for this study. After analysis, living specimens were released back into the bay.

Dark current appears as noise in the measurements. Dark current was removed by dividing the light sampled after connecting the fibre optic cable and light source, with the light sampled before connecting the fibre optic cable and the light source. The light source also has a distinct spectrum. Therefore, a submerged white reflectance standard (WS-1 diffuse reflectance standard, Ocean Optics Inc., Largo, USA, 99% reflectance within visible light) was measured between the samples and divided from the sample measurements using the "light spectrum" function in Ocean view according to equation 1.1 as described in Mogstad & Johnsen (2017).

2.3 *In situ* imaging

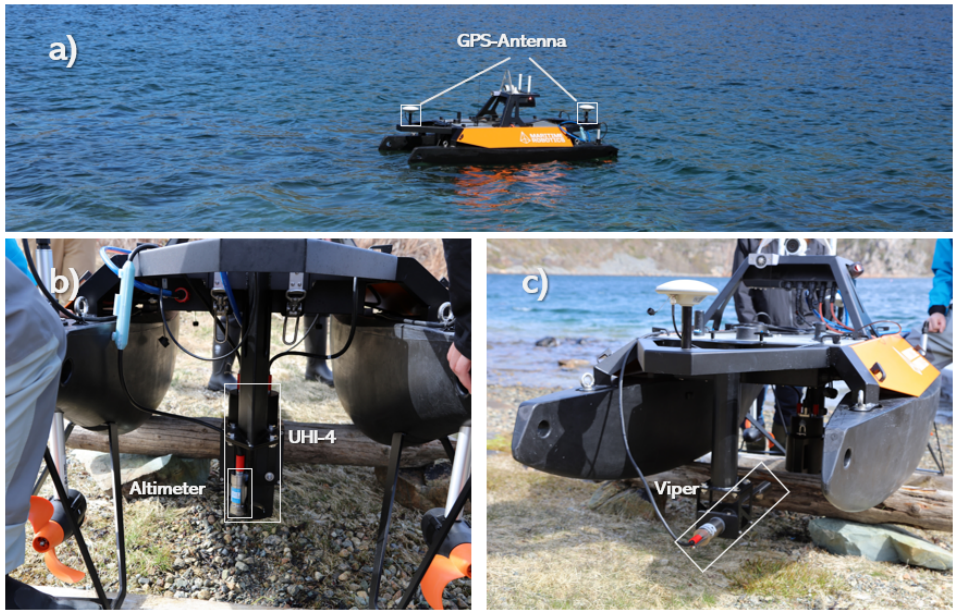

Figure 2.3: a) The unmanned surface vehicle (USV) mounted with two custom brackets to carry underwater payload sensors between its two hulls. b) At the back, a UHI is mounted to image the seafloor, with an acoustic altimeter which measures distance between camera lens and seafloor. c) At the front, a spectral light beam attenuation meter (Viper) measured light attenuation from 400 nm-700 nm. Photos by Asgeir Sørensen.

2.3.1 USV-based hyperspectral imaging

An Otter Pro USV (Maritime Robotics AS, Trondheim) carried a UHI-4 (Ecotone AS, Trondheim) in a similar setup to how it was done by Mogstad et al. (2019). A custom bracket was used to mount a Viper spectral light beam attenuation meter (TriOS, Germany) to the USV, and another bracket for the UHI, both instruments reaching approximately 40 cm below surface (figure 2.3). An antenna (airMAX LiteAP AC Access Point, Ubiquiti Networks, New York) was erected on the shore for communication between the USV and a computer on land. The computer allowed route planning and initiation, as well as manual steering of the USV (VCS, Vehicle control station, Maritime Robotics AS, Trondheim). The UHI was controlled from the same computer using the Immersion software (Ecotone AS, Trondheim), which allowed for adjusting exposure time, spectral and spatial binning as well as frame rate during the mission. Downwelling sunlight was the only source of light. A reflectance standard for visible ambient light was placed on the seafloor in the transect beforehand, which was used to register the spectral

downwelling irradiance, as well as the IOPs of the water, in post processing. The USV mission was initiated at 11:15 on September 9th. The velocity of the USV was set to a relatively high velocity of 1 knot in an effort to reduce the disturbance and movement from wind and waves. The photomosaics were captured with an exposure time of 40 ms, frame rate of 50 Hz (so as to match the high velocity), spectral binning was set to 4, reducing the spectral resolution to 2 nm, and the spatial binning set to 2, reducing the across track resolution from 1920 pixels to 960 pixels. Binning was done to reduce the size of the data sets, and allow for more light, hence a higher signal to noise ratio, in each pixel. The post-bin resolutions were considered adequate for the purposes of the study. As mentioned previously, the path of the USV was chosen beforehand, as part of Marte O. Sørengs study (figure 2.2).

Wind and waves have a significant effect on the position of the USV, this is a hazard when operating near shore. To avoid the USV drifting at the extremities of the transect line, the route start and end were planned safely away from shore, with a track that brings the USV gently into the transect line. This means the overlap between the USV and UAV transects extend the 48 meter line by some meters at each extremity. The total coverage of the USV photomosaic is approximately 120 m^2.

2.3.2 UAV-based hyperspectral imaging

A DJI S1000+ octocopter UAV (Operated by dept. of engineering cybernetics, NTNU) was fitted with an HI (SPECIM AFX10, Oulu, Finland) connected to a stabilizing gimbal gyroscope (Gremsy T7, Ho Chi Minh City, Vietnam) in the nadir viewing position (figure 2.4). The weather on the day of capture was cloudy and dry, with winds averaging 9 ms^{-1}, and the sun at an altitude of 16.3°above the horizon. The HI has a field of view (FOV) of 38 degrees and a spectral range from 400 nm to 1000 nm, with a spectral resolution of 5.5 nm. Most importantly, it covers the visible light range (400 nm to 700 nm). There are 1024 pixels in the cross track direction, and the HI has a 12-bit radiometric resolution providing 4096 levels of light intensity. Three missions (mission 1, 2 & 3) were operated across the same transect lines. For all three, the spectral binning was set to 2, spatial binning to 1, and target speed to 2 ms^{-1}. Previous test flights did not account for the difference in longitudinal and transverse sampling according to frame rate and altitude, resulting in elongated pixels and overall poorer quality in mapping. Flight and camera parameters were set so that the pixels at the ground are the same size in both dimensions (along-track and cross-track), resulting in square pixels (Table 2.1). For this to be true we assume that the UAV speed, altitude and attitude are constant throughout the transect. A reflectance standard of 1 m x 1 m was placed in the water, at a depth of approximately 2.5 m. An antenna was used for

Figure 2.4: The unmanned aerial vehicle (UAV, DJI S1000+) octocopter taking off, carrying the hyperspectral imager (HI, SPECIM AFX10) connected by a stabilizing gimbal (Gremsy T7), at Hopavågen. Photo by Pål Kvaløy.

communication between the field station (figure 2.2) and the UAV during flight. Routes are planned and initiated from base, and so is start/end of hyperspectral recording, and modification of exposure time and frame rate in flight. A route was planned along the shore covering the same area as the USV-transect, with margin. The UAV however ran for longer, approximately 600 meters aong the shore, while imaging. At sea level, the hyperspectral photomosaic hence covered an area of approximately 32 000 m^2 during mission 2. The photomosaic which covers the seagrass meadow is 200 meters long, and covers 10 800 m^2. The mission was initiated on March 4th 2022. It started at 10:27 and all three missions lasted until 12:08.

Table 2.1: Control parameters for the UAV and HI were set to match the along track pixel size with the cross track pixel size, at three different flight altitudes. All missions were performed on March 4th 2022.

	Mission 1	Mission 2	Mission 3
Time	10:27-10:45	11:22-11:35	11:52-12:05
Altitude (m)	147	74	111
Swath width (m)	102	51	77
Frame rate (Hz)	20	40	26.67
along track pixel size (cm)	10	5	7.5
cross track pixel size (cm)	10	5	7.5

Figure 2.5: An illustration showing the simultaneous hyperspectral mapping surveys performed in Hopavågen, Trøndelag. A USV travels as it images a seagrass meadow. The USV cayrring a UHI survey was synchronized with the UAV carrying a HI transect above the seagrass meadow, and the two transects are compared in the results. Photomontage, photos by Pål Kvaløy and Asgeir Sørensen.

2.4 Data processing

2.4.1 USV-UHI data processing

USV photomosaics were automatically georeferenced in Immersion, using navigation data from the USV. radiometric correction was performed according the method described by Marte O. Søreng (2022) & Mogstad et al. (2019). Raw data photomosaics from the UHI was converted to radiance L(λ) using Immersion. Photomosaics were then opened in ENVI (Environment for Visualizing Images, v. 5.4; Harris Geospatial Solutions Inc., Boulder, USA), where they were converted to reflectance using the "Flat field correction" tool, according to equation 1.1 an example of this process is seen in figure 2.6.

2.4.2 UAV-HI data processing

The inertial measurement unit (IMU) of the HI was not turned on during the March flight, hence proper geographical referencing was not possible. However, the UAV photomosaic was of such high quality that landscape features were clearly visible. It was therefore manually georeferenced using an affine transformation in the "Georeference" tool in ArcGIS, based on comparison of landscape features between UAV photomosaic and ortophoto from Kartverket (2019).

Each transect of the UAV photomosaic were stored as separate files in the band

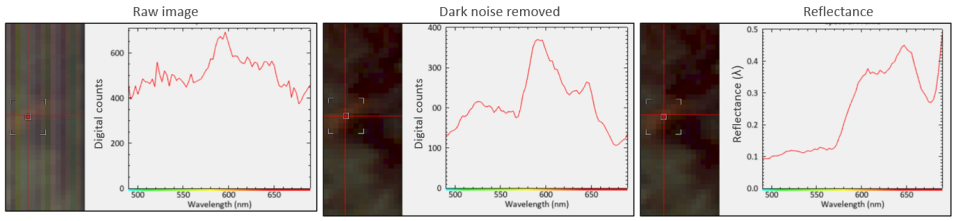

Figure 2.6: Three panels showing a pixel covering a red algae from the UAV photomosaic (Raw image, dark current removed and reflectance converted). The first image is the raw spectral upwelling reflectance data. The second panel is the raw image, but the average dark current has been subtracted for each wavelength and along track line. In the third panel, the IOPs have been removed by dividing the photomosaic by the R(λ) of the reflectance standard. The full transect length is approximately 60 m, with the panels snapping approximately 10 m each.

interleaved by lines (BIL) file format. With radiometric intensity stored as digital counts (0-4096 in the 12-bit imager). The raw data is often converted to radiance with a previously prepared calibration data specific to the sensor. The radiance converted photomosaic is then converted to reflectance photomosaic using the color of the white reflectance standard (figure 2.6, Johnsen et al. (2013), Mogstad & Johnsen (2017), Mogstad et al. (2019)). Radiance conversion was not possible for the UAV photomosaic. 100 frames at the end of each transect were captured with the shutter closed, to capture the dark current. The dark current is specific for each along track line, so the average value of the dark pixels at the bottom of each along track line was subtracted from each line, producing a picture of spectral light intensity. Subsequently, pixels at the center of the reflectance standard were sampled using the "Region of interest (ROI)" tool in ENVI. The spectra of all pixels in the transect were then divided by the average spectral intensity values of the ROI using the "Flat field correction" tool. The resulting transect shows relative reflectance (*R*). It is important to note that the reflectance standard was placed at a relative depth of 2.5 meters, meaning the whole transect is corrected for the IOPs at this depth. This is a result of using the "flat bottom assumption" (Rubasingam et al. 2011).

2.5 Sampling and SAM classification in the USV & UAV photomosaics

Red algae, brown algae, seagrass and sediment were sampled for the three methods used in this study, i.e.*In vivo* spectrometry (R(λ)),*In situ* USV and *In situ* UAV photomosaic. From spectrometry, there were 70 samples of red algae, 56 samples of brown algae, 5 samples of seagrass and 6 samples of sediment. From the USV

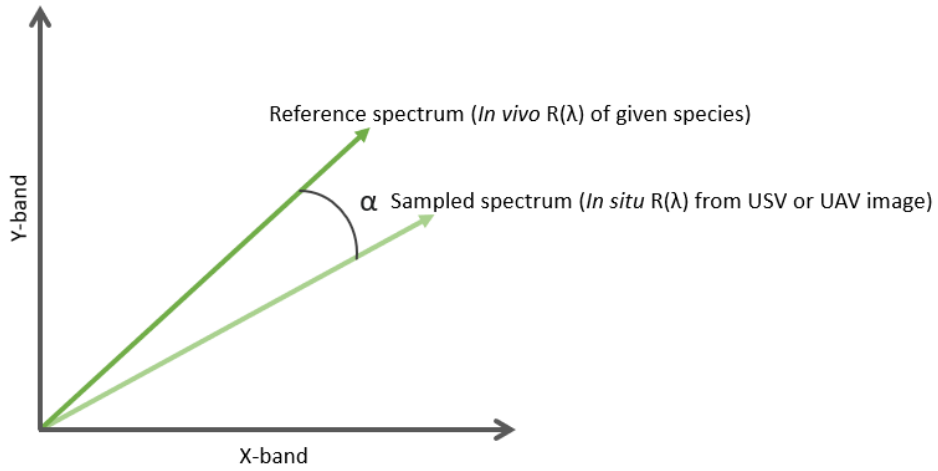

Figure 2.7: The spectral angle (α) is calculated according to equation 2.1 and gives the n-dimensional angle between the reference R(λ), measured using spectrometer and the sample R(λ) from the USV or the UAV photomosaic, where x and y bands represent color bands. This is a 2D representation of the n-dimensional vectors. Adapted from Kruse et al. (1993)

photomosaic and the UAV photomosaic, 100 pixels were manually sampled from each class. Classes were sampled based on appearance, spectral signature, and physical surveys, giving first hand knowledge of present species. As different spectrometry sensors capture light at different spectral intervals and ranges, all classes were resampled to fit the overlapping range from 490 nm to 690 nm, at 1 nm intervals, using the "spectrolab" package in Rstudio (RStudio Team 2022, Meireles et al. 2017), and plotted with standard deviance for comparison. The n-dimensional spectral angle (α, figure 2.7) of each class from the USV photomosaic and the UAV photomosaic were calculated from equation 2.1 (Kruse et al. 1993), where α is the spectra angle, n is the number of spectral bands, t is the sampled R(λ) sampled *In situ* and r is the reference R(λ) measured *in vivo* with the spectrometer. Light intensity of a sample is irrelevant, as equation 2.1 normalizes the spectra to calculate the angle. The α was used as an estimate of difference between spectrometry R(λ), and *In situ* R(λ). The α was then used to perform a spectral angle mapper (SAM, Kruse et al. 1993) classification on the transects.

$$\alpha = cos^{-1}\left[\frac{\sum_{i=1}^{n} t_i r_i}{\sqrt{\sum_{i=1}^{n} t_i^2}\sqrt{\sum_{i=1}^{n} r_i^2}}\right] \tag{2.1}$$

2.5.1 Accuracy assessment of SAM classification

The SAM classified transect was inspected to verify the classification accuracy. A confusion matrix comparing manually classified ROIs and SAM classification was made to asses the accuracy of the SAM classification. 500 random pixels were chosen within both photomosaics (USV & UAV) in ENVI. Each pixel was manually classified by an expert, only based on the spectral signature, as one of the four classes (red algae, brown algae, seagrass & sediment), or as unclassified. For each pixel, their SAM classification and manual classification were compared in a confusion matrix. This resulted in a total percentage of the chosen pixels which were put to the same class by SAM and manual classification. Here, 100% means both classification methods are in complete agreement, and 0% means there is no agreement (further details, see Rossiter et al. 2020). The total percentage of pixels which were classified differently between SAM and manual classification is the error assessment of the SAM-classification. This methods assumes that manual classification is correct.

Chapter 3

Results

3.1 Transects

3.1.1 USV photomosaic and manual sampling of pixels

The USV photomosaic was georeferenced with a spatial precision of 40 cm. Preliminary investigations of the transect revealed R(λ) from the species observed from underwater RGB footage and snorkeling, indicating that the spectral signal is good. Seagrass looks very dark in the transect. The samples of seagrass pixels look very different to the spectrometer samples. However, the distinct reflectance peaks of seagrass around 550 nm and 630 nm are clearly visible. Brown algae also deviates from the spectrometer measurements. Finding pixels that look similar to the spectrometer measurement of brown algae was difficult, but the average R(λ) of the sampled pixels (figure 3.6) shows the distinct reflectance peaks of brown algae. The sediment and red algae in the USV transect were easy to sample and generally showed R(λ) similar to those observed in the spectrometer measurements (figure 3.1).

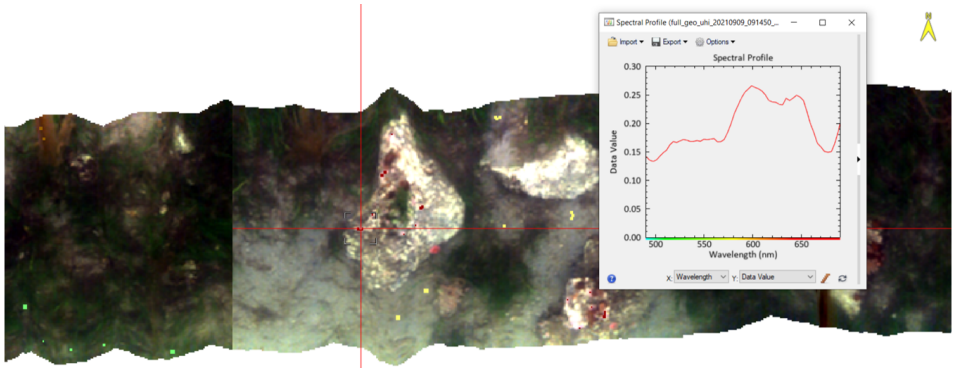

Figure 3.1: Pixels from the USV photomosaic were manually sampled in post processing using the "ROI" tool in ENVI. Red pixels are red algae, yellow are sediment, green is seagrass and brown are brown algae. The chosen pixels show a red algae.

3.1.2 UAV photomosaic and manual sampling of pixels

The lowest altitude mission was chosen for the UAV (Mission 2, table (2.1), as it had the highest spatial resolution. While mission 1 was the only available photomosaic of Straumen, covering the brown algae. The UAV photomosaic is underexposed, with benthic signatures at depths below 2 meters all share a similar R(λ), which were generally flat but with wave-like variations caused by noise. The high level of noise at the depths interesting to this study (1-5 m, where the classes are mainly found) make the classes of interest difficult to discern. The red algae in Hopavågen are located in the hydro-littoral (figure 2.1). Making sampling of red algae pixels easy with red algae reflectance peaks at 600 nm and 645 nm clearly visible (figure 3.2). Sediment, brown algae and seagrass were only discernible due to underwater RGB footage from the same area, and experience from snorkeling during sampling and preparation. The sampled pixel averages for sediment, brown algae and seagrass contain much noise, with reflectance peaks being difficult to recognize.

3.1.3 Pixel based comparison of the USV and UAV photomosaic

The USV photomosaic was georeferenced according to navigation data captured by the USV during the mission. It was however not possible to georeference the UAV photomosaics automatically. With little movements in the UAV, and natural features easily recognizable, its is possible to discern the classes of interest. Minor discrepancies in the photomosaic are results of movement in the UAV during flight (figure 3.3). Despite having manually georeferenced the UAV photomosaic, minor imprecisions in georeferencing of both photomosaics, and unevenness caused by minor movements in the vehicle may leave several meter offset between the two

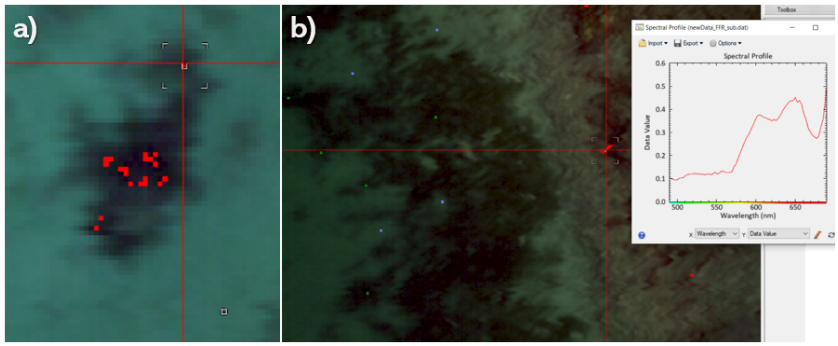

Figure 3.2: a) sampling of pixels from the UAV photomosaic a cluster of brown algae near Straumen in flight line 2 (figure 2.2) using the "ROI" tool in ENVI. b) Using the "ROI" tool to sample pixels of red algae from the UAV photomosaic, where red algae are colored red, sediments and seagrass blue and green respectively.

transects, rendering a pixel by pixel comparison hard to obtain.

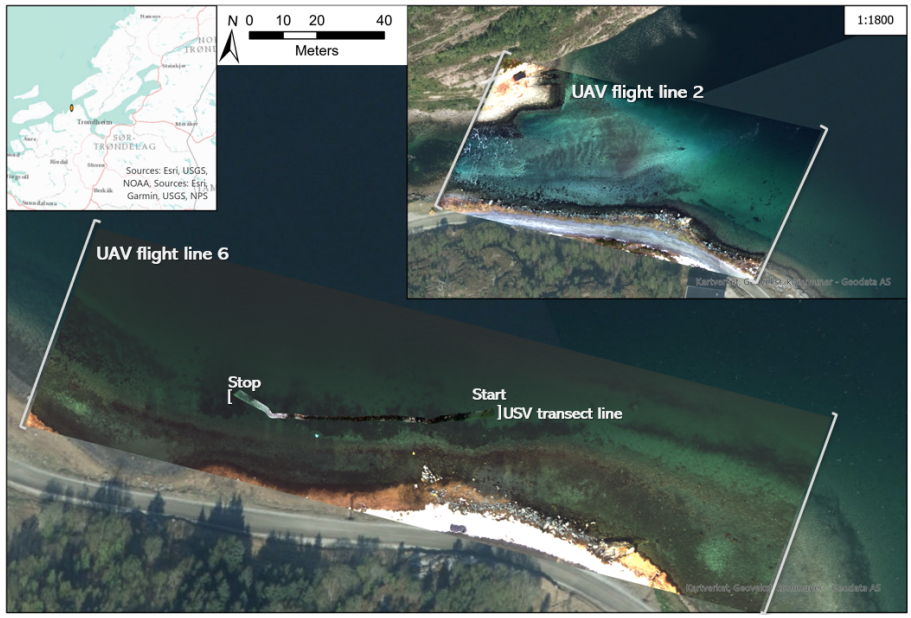

Figure 3.3: USV photomosaic was georeferenced according to navigational data from the USV, while UAV photomosaic (flight line 6) was georeferenced based on known points on an ortophoto layer (Kartverket, 2019). The top right map shows flight line 2, also georeferenced according to known points, while the top left map shows the position of Hopavågen near the mouth of the Trondheimsfjord.

3.2 Spectral reflectance of classes sampled *in vivo*, from USV, and from UAV

3.2.1 Seagrass

The dominating pigments of seagrass are clearly visible in the spectrometry and UHI samples with peak reflectance at 550 nm & 630 nm (figure 3.4). The α between the UHI-seagrass and the spectrometer seagrass at 27° (table 3.1) is evidence of a lot of variation within seagrass spectral signatures. Table 3.1 shows the seagrass from the UAV photomosaic compared to the seagrass measured using spectrometry has a spectral angle of α=39°. Seagrass samples from the UAV photomosaic show no characteristics of the spectral signature that is expected from seagrass as measured in the lab (figure 3.4). During ROI-sampling, seagrass was relatively easy to spot as snorkeling and footage had given first hand knowledge of the seagrass location and extent.

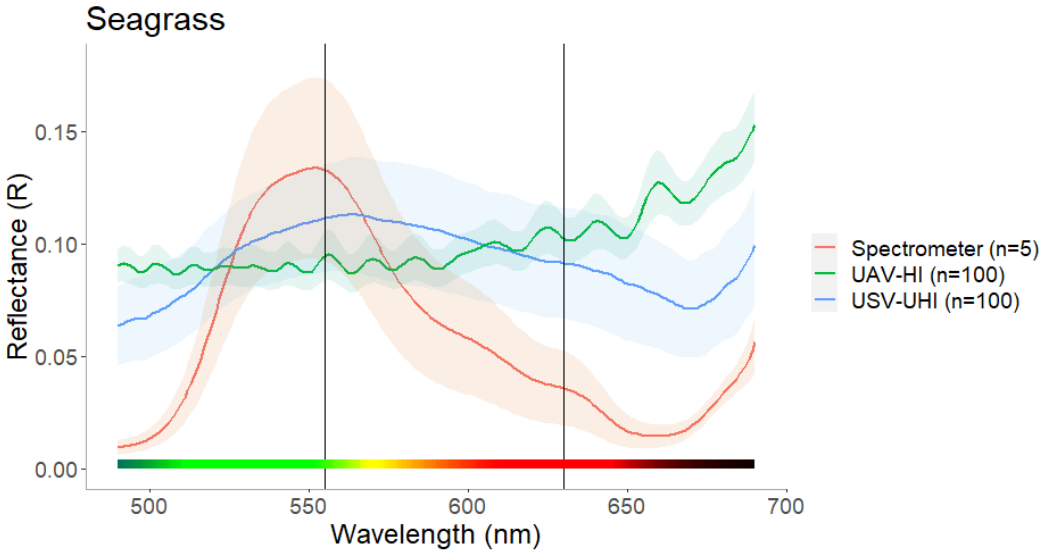

Figure 3.4: Spectral reflectance of seagrass as measured by *In vivo* spectrometer (n=5), *In situ* UHI (n=100) and *In situ* HI (n=100) between 490 and 690 nm. The lines show the average of all samples, while the shaded area cover the $\pm$ SD of mean. Vertical lines show reflectance peaks caused by low pigment absorption.

3.2.2 Red algae

All methods produce a similar R(λ), the α between the R(λ) are relatively small. The α between the USV photomosaic red algae and the spectrometer red algae is 9°. While the α between the UAV photomosaic red algae and the spectrometer red algae is 11° (table 3.1). Within the range of 490 nm to 690 nm red algae has two distinct reflectance peaks, at 600 nm and 645 nm as measured with the spectrometer. The reflectance peaks are present in all R(λ)s. The R(λ) from the UAV photomosaic (green line in figure 3.5) however has a red shift, of about 5 to 10 nm, as well as an upward tilt of the general R(λ) towards the red light. Red algae in the UAV photomosaic was sampled from depths of 0.5 m to 1 m as these areas contained the only distinguishable and concentrated samples of red algae in the UAV photomosaic.

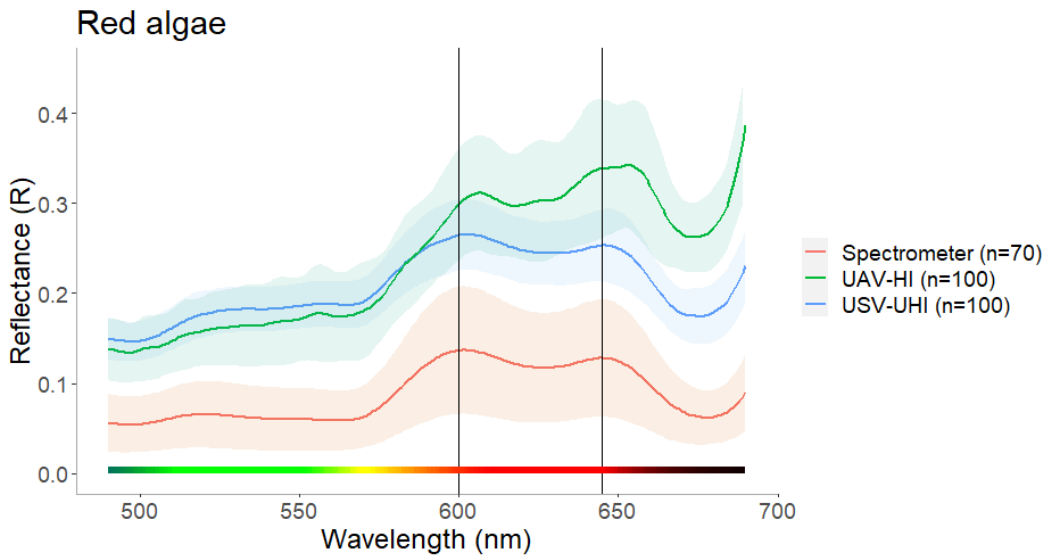

Figure 3.5: Spectral reflectance of red algae as measured by *In vivo* spectrometer (n=70), *In situ* UHI (n=100) and *In situ* HI (n=100) between 490 and 690 nm. The lines show the average of all samples, while the shaded area cover the ± SD of mean. Vertical lines show reflectance peaks caused by low pigment absorption.

3.2.3 Brown algae

The α between the UAV samples of brown algae and the spectrometer measurements of algae is large (α=24°). While the angle between the USV sample and the spectrometer measurement is smaller at α=7°(table 3.1). The spectrometer measured brown algae have distinct reflectance peaks at 600 nm and 645 nm, as well

as a peak at 570 nm, which separates it from red algae. In figure 3.6 the green line (UAV-HI) has been normalized to visualize the peaks and troughs of the other R(λ)s for better comparability. The green R(λ) (figure 3.6) shows no distinct peaks at 570 nm, 600 nm or 645 nm. Like with seagrass, it would be impossible to confirm that this is brown algae without first hand knowledge from ground truthing, such as underwater videos of the area and snorkeling.

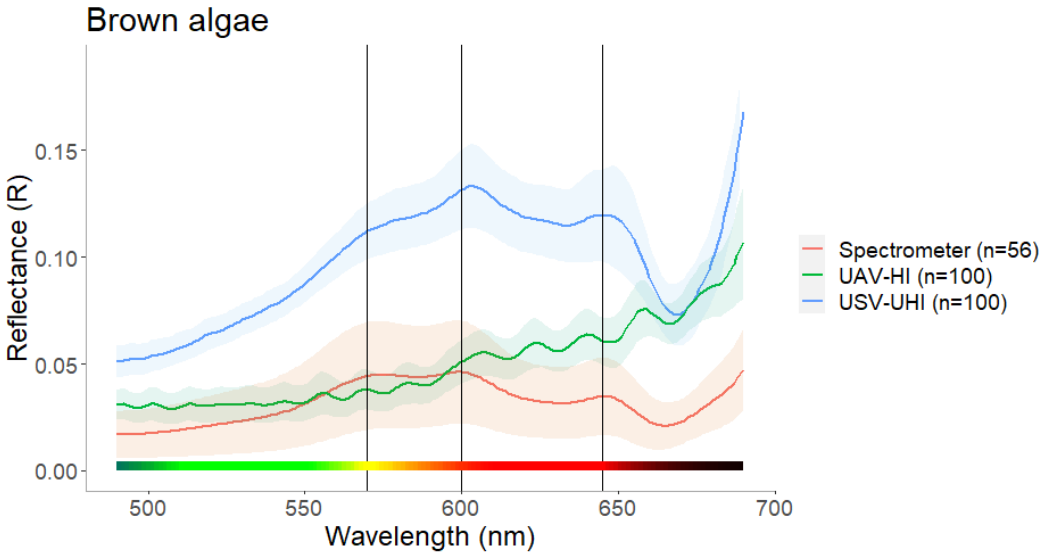

Figure 3.6: Spectral reflectance of brown algae as measured by *In vivo* spectrometer (n=56), *In situ* UHI (n=100) and *In situ* HI (n=100) between 490 and 690 nm. The green line (UAV-HI) has been normalized. The lines show the average of all samples, while the shaded area cover the ± SD of mean. Vertical lines show reflectance peaks caused by low pigment absorption.

3.2.4 Sediment

The general R(λ) from the UAV photomosaic sediment is similar between the USV photomosaic and spectrometer, giving a small α of α=3°(table 3.1) between both the USV and UAV sediment, and the spectrometer sediment. The sediment R(λ) are generally flat, with gentle sloping from 550 nm down to 400 nm, and down from 550 nm to 670 nm. It has a vague peak around 550 nm similar to that of seagrass. With a vague trough at 670 nm, and a gentle rise beyond 670 nm. These characteristics are shared between all R(λ) in figure 3.7. The same noise that is observed in the brown algae and seagrass from the UAV photomosaic also occurs in the sediment.

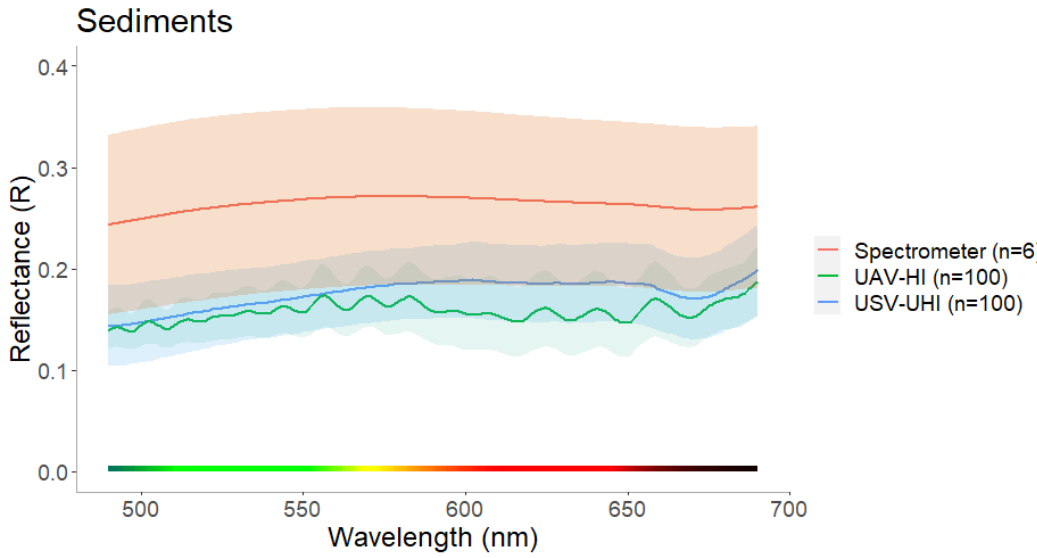

Figure 3.7: Spectral reflectance of sediment as measured by *In vivo* spectrometer, *In situ* UHI and *In situ* HI between 490 and 690 nm. The lines show the average of all samples, while the shaded area cover the ± SD of mean.

Table 3.1: 100 pixels of each class were manually sampled from the USV photomosaic and the UAV photomosaic. The spectral angle (α) between each class and the corresponding class from spectrometry were calculated according to equation 2.1. The resulting angles show how different the *in situ* spectra, as seen from UAV and USV, are from the spectra measured *in vivo* using the spectrometer.

	Red Algae	Brown Algae	Seagrass	sediment
USV-UHI	9°	7°	27°	3°
UAV-HI	11°	24°	39°	3°

3.3 Spectral Angle Mapper Classification

3.3.1 USV photomosaic classification

A SAM classification was applied to the USV-UHI photomosaic with the calculated α (table 3.1) as parameters (figure 3.8). The SAM-classification in the USV photomosaic (figure 3.8) of brown algae classified many pixels correctly. In panel a, several brown algae (dominated by *F. serratus*) were classified as red algae in single pixel spots. Other brown algae along the transect (likely *C. filum*) were however mostly classified correctly. A large area classified as brown algae in panel b

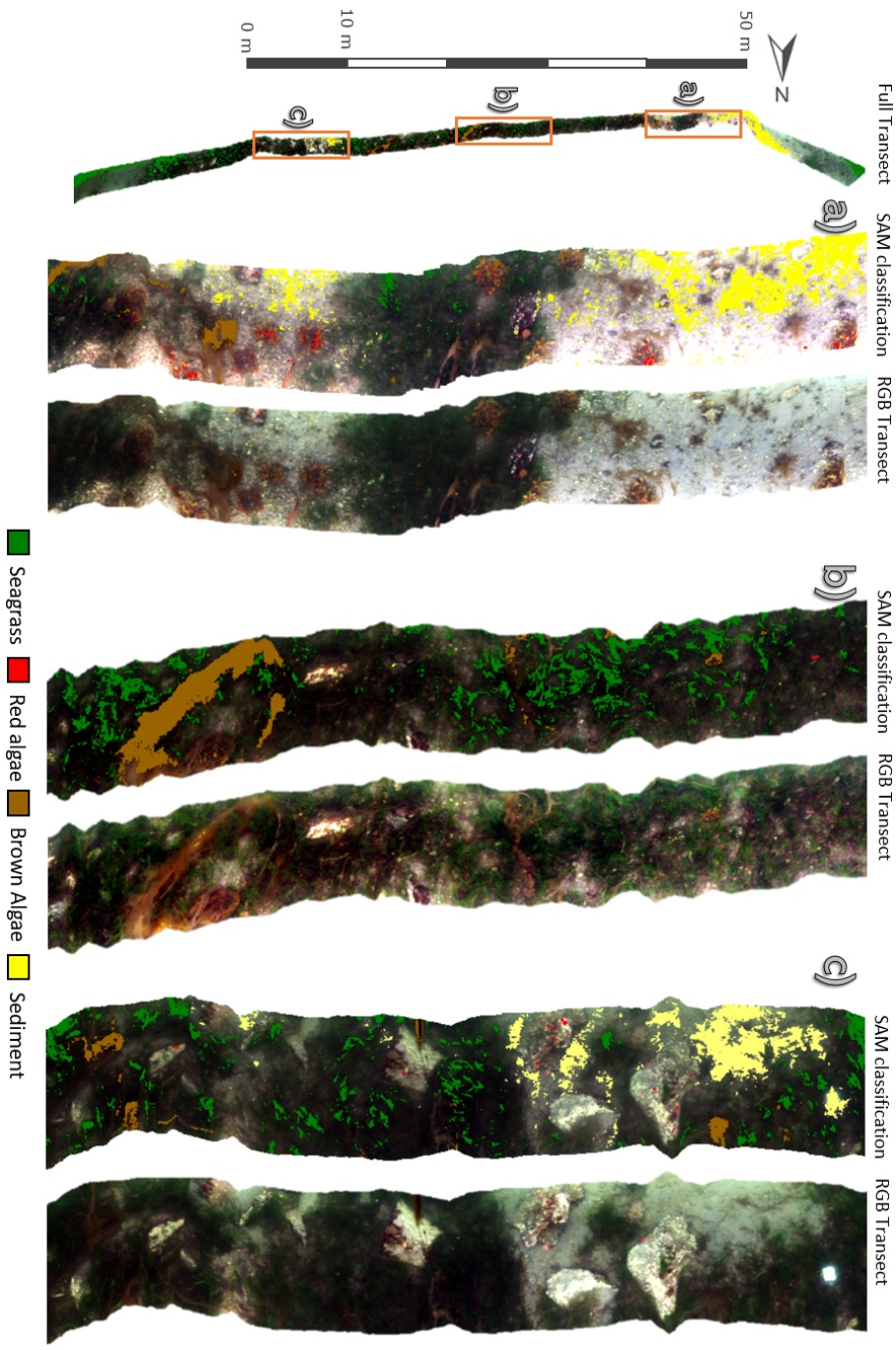

Figure 3.8: A SAM classification was applied to the USV photomosaic for the four classes (Seagrass, Red algae, Brown algae and Sediment), using the calculated spectral angle (α, table 3.1). Three areas of interest are displayed (a, b and c), and their position in the transect is shown in the overview map to the left.

seems to contain a mix of both brown algae and seagrass. Occasional sediment classification appear to cover rocks and sediment.

Pixels classified as sediment (figure 3.8) are mainly classified correctly, but sediments are generally under-classified (panel a). Only the pixels which appear to be "pure" of spectral mixing seem to be classified as sediment. After correction, the reflectance standard had a flat R(λ), not unlike that of the sediment, and has hence been classified as sediment by the SAM classifier.

Seagrass is significantly under-classified in the whole transect (figure 3.8. In panel a, there is a cluster of seagrass in the midlde, of which only a small portion is classified. The rest of the transect contains significant dark patches of seagrass, where little is classified as such. In panel b and c, some seagrass is incorrectly classified as brown algae. At the start and end of the transect, much of the sediment is classified as seagrass. The photomosaic is wider here, meaning it is also deeper (>2.5 m deep) than the rest of the transect.

Red algae occur on smaller clusters, on hard substrates. Red algae are generally classified correctly on the interspersed rocks in the seagrass meadow (figure 3.8 b,c). In panel a, some brown algae are classified as red algae. Manual inspection of the R(λ) of these pixels reveal the characteristics of red algae, suggesting there are epiphytic red algae on the brown algae (Kersen et al. 2011).

3.3.2 UAV photomosaic classification

The UAV photomosaic was characterized by a low signal to noise ratio at depths beyond approximately 2 m. The Sediments were classified well at the same depth as the seagrass meadow and the reflectance standard (2.5 m depth). To the left the classified sediments slowly obscure into classified seagrass, along a line which matches well with where the sediments slope down from 2.5 m to 4 meters outside of the seagrass meadow (figure 3.9). All pixels beyond this slope is classified as seagrass. The reflectance standard is also classified as sediment.

The seagrass meadow as is correctly classified as seagrass. However, severe over-classification of seagrass (figure 3.9) in other areas indicate that the classification is very inaccurate (table 3.3). The correctly classified seagrass can only be confirmed when comparing the full photomosaic with ortophoto and simultaneously captured underwater RGB footage. Again, none of the investigated seagrass classified pixels showed any of the distinct reflectance peaks of seagrass. Most of the water which was not classified as sediment were classified as seagrass, as well as certain pixels on land.

Red algae were classified with high accuracy. Few pixels were classified. There-

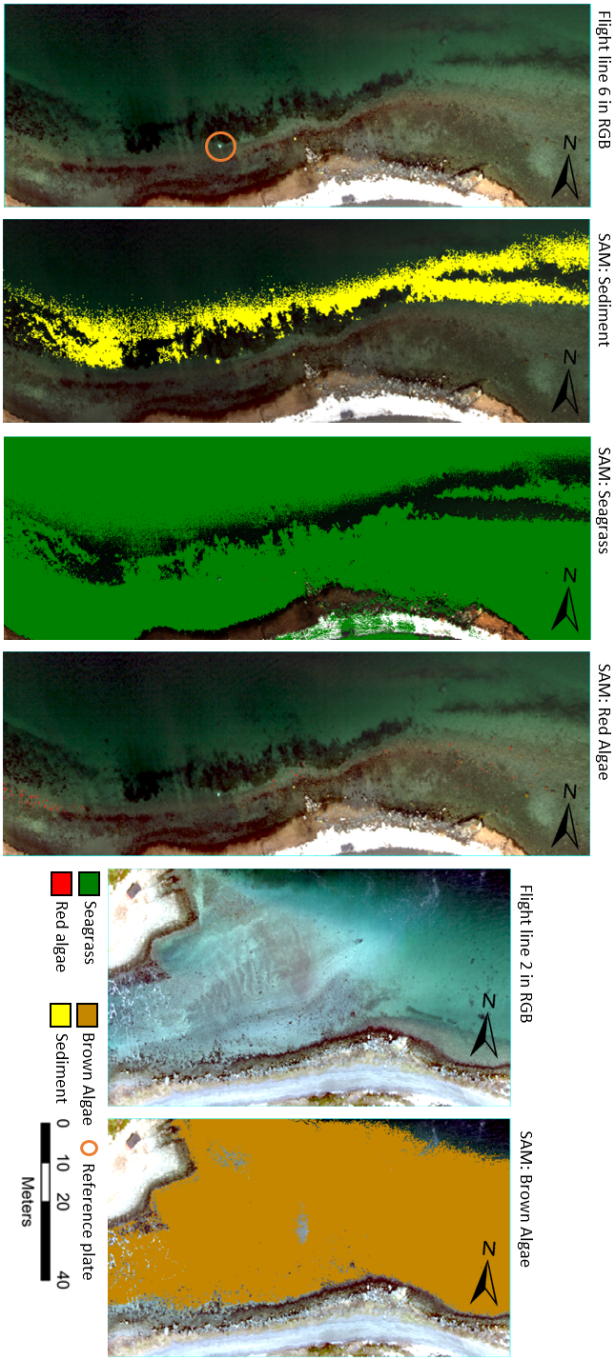

Figure 3.9: A SAM classification overlaid the RGB representation of UAV-HI flight line 2 and 6 (figure 2.2). The calculated spectral angle (α, table 3.1) were used as parameters. The first four photomosaics show flight line 6, in which sediment, seagrass and red algae were classified. The last two photomosaics show flight line 2, in which brown algae were classified.

fore, most were investigated and showed the distinct R(λ) of red algae. Certain pixels which were not classified also showed spectral characteristics of red algae in the surrounding areas. Suggesting that the α is to small, and red algae are under-classified.

Brown algae were not classified in the seagrass meadow (flight line 6). There were no large clusters of brown algae along the seagrass meadow, hence classification of brown algae was not expected either. It was instead classified near Straumen (figure 3.9). Brown algae classification misclassified much of the sediments and other features, similar to how seagrass did. It is however more modest, due to the smaller α than seagrass classification. Neither the shoreline nor the deeper water classified as brown algae.

3.3.3 Accuracy assessment of SAM classification

Table 3.2: USV-UHI confusion matrix comparing the manually classified pixels (first row in table) with the class assign by SAM (first column in table). The bold numbers show the percent of pixels which were put to the same class where the total sum of each column is 100%. n=500.

	Unclassified	Seagrass	Red algae	Brown algae	Sediment	Total
Unclassified	**86%**	49%	38%	29%	61%	
Seagrass	11%	**51%**				
Red Algae			**62%**			
Brown algae				**71%**		
Sediment	3%				**39%**	
						63.4%

For USV, 63.4% of total chosen pixels were put to the same class when classifying manually, as with the SAM classification. Out of the 500 pixels inspected, only 2.8% of SAM classified pixels gave a false positive. 100% means SAM and manual classification agree on the class of all pixels.

Table 3.3: UAV-HI confusion matrix accuracy assesment similar to table 3.2. The bold numbers show the percent of pixels which were put to the same class. n=500.

	Unclassified	Seagrass	Red algae	Brown algae	Sediment	Total
Unclassified			12%			
Seagrass	54%		83%		6%	
Red Algae			**5%**			
Brown algae	46%					
Sediment					**94%**	
						24.8%

For UAV, 24.8% of chosen pixels were put to the same class when classifying manually, as with the SAM classification. 25% of classified pixels were false positives, classified as seagrass and brown algae. Out of the 500 pixels inspected, 67% of SAM classified pixels gave a false positive.

Chapter 4

Discussion

This study is a part of the infrastructure project SeaBee. Where the aim is to develop necessary equipment, knowledge and training to map nature types along the Norwegian coast using UAV based imagers. This study applied the newly aquired Specim AFX10 HI, and the combination with previous information and methods to map benthic marine nature types according to NiN using the supervised classification method SAM. The study has had a special emphasis on SAM classification, and its parameter, called the spectral angle (α), as SAM is a simple and common tool used in hyperspectral photomosaic classification (Nababan et al. 2021, Rossiter et al. 2020, Flynn & Chapra 2014). Supervised SAM classification from the USV photomosaic was found to have an accuracy of 63.4% when compared to manual classification, whereas supervised SAM classification from the UAV photomosaic obtained an accuracy of 24.8% when compared to manual classification.

4.1 Transects

4.1.1 USV based UHI photomosaic

The USV photomosaic had an estimated pixel size of 1 cm^2, and can in theory capture anything larger than this with relative certainty. The seagrass leaves sampled from Hopavågen in May and September were commonly 2-4 mm wide. The great three-dimensionality of the seagrass meadow canopy casts shades. This means any single pixel contains a mix of seagrass leaves at different depths with different levels of shade and different angles relative to the lens (Dekker et al. 2007) meaning all seagrass-pixels are expected to be spectrally mixed. With the USV photomosaic captured on September 9th, seagrass are expected to have near annual peak pigment content (Alvsvåg 2017). Meaning the distinctive reflectance

peaks for each class should be especially easy to observe. The USV photomosaic is in general of high quality with R(λ) of classes clearly distinct. With decent geographical referencing accuracy of 40 cm and appropriate color intensity range for most classes observed.

4.1.2 UAV based HI photomosaic

The UAV photomosaic showed a low signal to noise ratio across most of the seafloor. Most features below water were covered up by spectral noise. As the sun was only 16.3° above the horizon during the UAV mission on March 4th, a mission in the spring/summer season would see substantially more available light. The set exposure time was likely too short to capture a significant signal (figure 3.1) over the area of interest. The dept. of cybernetics, NTNU has also mentioned unresolved issues with the calibration of the HI, which may be the cause of the wave-like noise observed over large parts of the photomosaic, and also from the classes sampled in the UAV photomosaic (figure 3.4,3.6,3.5,3.7). It has been suggested that the exposure time should be increased for further studies, and that further studies are done in the spring/summer seasons.

There is an issue with assuming a flat bottom for a photomosaic captured from a UAV. Håvard S. Løvaas (dept. of Marine technology, NTNU) is currently using simultaneously captured photos for estimating the water depth in the transect. The aim is to apply water attenuation measurements to perform depth dependent radiometric correction. However, as no such method is available yet, radiometric correction of the UAV photomosaic relied on the flat bottom assumption (Rubasingam et al. 2011). Which is a common method for correction of IOPs when using UHI (Johnsen et al. 2013, Mogstad & Johnsen 2017, Summers et al. 2022, Montes-Herrera et al. 2021). While a flat bottom was assumed for radiometric correction of the UAV photomosaic, this is obviously not the true case, with depths ranging from land to 9 m deep seafloor. Water attenuates light exponentially towards red wavelengths with depth, areas shallower than the reflectance standard will have an overemphasized reflectance of red light after radiometric correction (Smith & Baker 1978). This effect can be seen for the red algae sampled in the UAV photomosaic (figure 3.5). Areas deeper than the reflectance standard will show a stronger influence of the IOPs, with increasing attenuation of the red wavelengths. In this UAV photomosaic however, the noise generally exceeds the signal strength at depths including and deeper than the reflectance standard. Because of this, reflectance peaks are hard to detect for all classes beyond 2.5 m deep. It is yet unclear at what maximum depth one can reliably hope to record spectral signatures of the seafloor. According to Vahtmäe et al. (2006) it may be possible to register spectral signatures down to 10 m depth in clean coastal water from a UAV.

4.1.3 Pixel based comparison of the USV and UAV photomosaic

A pixel based comparison of the USV photomosaic and the UAV photomosaic would provide an opportunity to describe the spectral mixing which occurs in the pixels of the UAV photomosaic, which has a poorer spatial resolution, hence covering a larger area on the ground. SAM classification assumes that all pixels are "pure", as in there is no spectral mixing (Rashmi et al. 2014). This methods sheds light on the spectral mixing effects and allows for analyzis of specific spectra components. The procedure for a pixel based comparison of the two photomosaics would be as follows: The two transects would be imported and overlaid using ENVI. Several areas corresponding to 7x7 pixels in the USV photomosaic would be chosen, as such an area is guaranteed to cover at least one pixel size in the UAV photomosaic given the pixel resolution in this study. One could then calculate the α between each of the 49 pixels from the USV photomosaic and the corresponding pixel(s) covering the same area in the UAV photomosaic, as a quantitative measure of the difference of the $R(\lambda)$ between the large pixel of the UAV photomosaic and its component pixels from the USV photomosaic.

This method does however assume that the geographic referencing precision of both photomosaics is done with a very high precision, and that the two transects are captured at the same point in time, at least during the same day. It also assumes that the radiometric correction has been successful in removing any significant influence of the IOPs, and that there is a flat bottom in both transects. For this study, none of these assumptions were true, hence this method was not performed. The lack of automatic geographical referencing dramatically reduced the accuracy of the transect and rendered a pixel by pixel comparison useless. The unfortunate lack of IMU data from the flight has been mentioned as an important reminder for future studies. The precision of both vehicles positioning data could also be improved using publicly available RTK (real time kinematic) positioning-data from Norwegian Mapping Authority. With better preparation, the USV and UAV photomosaics should also be captured simultaneously. Lastly, for the area (approx. 120 m^2) covered by the USV, it is reasonable to assume a flat bottom in both photomosaics.

4.2 Spectral reflectance of classes sampled *in vivo*, from USV, and from UAV

4.2.1 Seagrass

Species from most algal phylum cover the seagrass leaves, but red algae generally dominate in both composition and biomass (Alvsvåg 2017, Larkum et al. 2006, Borowitzka et al. 2007). Epiphytic red algae may explain the red shift of the reflectance dip around 670 nm, in seagrass captured by the USV (figure 3.4). Diverse epiphytic organisms also diminish specific reflectance peaks, especially in the 575 - 630 nm region (Fyfe 2003). During physical sampling, withered leaves were also found mixed in the seagrass meadow. The USV photomosaic was captured in September, when pigment content of seagrass is near its seasonal peak (Alvsvåg 2017). This array of factors in spectral mixing may explain why the large α within the different samples of the seagrass pigment class (table 2.7) compared to the other pigment classes.

The poor R(α) signal resulting from a combination of low signal to noise ratio and a low pigment concentration will be mitigated by imaging seagrass in the spring/summer. The UAV photomosaic was captured in March, when the pigment content of seagrass is near the annual low, and pigment composition is differerent than in the summer (Guidetti et al. 2002, Moore & Short 2007). With seagrass having a generally low reflectance, i.e. absorbs a lot of light, seagrass near optically deep water is also difficult to observe.

None of the analyzed pixels in the UAV photomosaic contained a R(λ) characteristic to seagrass. Sampling seagrass-pixels in the UAV photomosaic would therefore be very difficult without detailed knowledge of the area. The high α of 39°(table 3.1) for seagrass sampled from the UAV photomosaic shows that there are few similarities between the R(λ) from the UAV photomosaic and the spectrometer (see figure 3.4).

The seagrass sampled for the spectrometer were free of epiphytes, and measured at the healthy and green part of the leaves. To improve the spectrometer sample, one could include a broader diversity of leaves, which more closely reflects the natural composition of the meadow and hence better classify the nature type. Combining classification with publicly available depth and tide data would separate M7 1 & 3 (hydrolittoral) from M7 2 & 4 (sublittoral). Finally, including field sampled salinity data would allow for determination between all classes. It is beneficially to maximize the amount of information extracted from the data set as field mission are expensive and time consuming (Rinde et al. 2021).

4.2.2 Red algae

Red coralline algae are even in shape, and encrusting to the substrate. It is a hard biofilm that does not move with the watermasses like seagrass and brown algae. Red algae appears flat compared to the structurally complex seagrass and brown algae. Red algae also generally cover areas larger than the pixel size, usually giving several adjacent pixels with R(λ) characteristic to red algae.

The USV photomosaic is intentionally captured over a seagrass meadow, consisting of mostly loose sediments, hence the low occurrence of red algae. Red algae mainly occur in the shallow parts of the bay, where rocks provide stable substrate, this is also where red algae are observed in the UAV photomosaic. The right side upward tilt in the R(λ) of red algae (green line in figure 3.5) is likely caused by the algae being less deep than the reflectance standard (figure 3.9). Areas less deep than the reflectance standard will have an overestimation of the attenuation of red light after radiometric correction. The red shift of the peaks sampled from the UAV photomosaic might stem from seasonal changes in the pigment composition of red algae (Leukart 1994).

The α between red algae samples are small compared to seagrass and brown algae. Red algae and sediment are more likely to overcome noise, As they are brighter than seagrass and brown algae. By observing the percentage of reflected light for each class (figures 3.4,3.5,3.6,3.7) it is apparent that red algae and sediment reflect more light than seagrass and brown algae. While seagrass and brown algae have a peak reflectance around 15% (R=0.15), red algae and sediment have a peak reflectance around 30% (R=0.30).

The red algae used as spectrometer samples contain a mix of leafy red algae and coralline red algae, which have a slightly different R(λ) (Hochberg & Atkinson 2003). The NiN nature types organized as "red algae" however, only contain coralline red algae. The spectrometer sample could be improved by excluding leafy red algae. The environmental variables differentiating between optically shallow nature types M1 and M4, and types within M4, describe substrate grain size, substrate composition and salinity. Qualified NiN personnel and field sampling is therefore required if one wishes to determine between the nature types within the red algae pigment class.

4.2.3 Brown algae

Brown algae samples are 7° and 24° (USV and UAV respectively) different to the spectrometer samples. Like seagrass, brown algae observed in Hopavågen are characterized by three-dimensional complexity and thin leaves (some species) giving a high degree of spectral mixing between illuminated, shaded leaves and

the substrate, at different distances and angles to the lens (Rossiter et al. 2020, Fearns et al. 2011). The brown algae in Hopavågen also peak in photosynthetic productivity during summer, and are photosynthetically inactive during the winter months (Yokohama 1973, Wiencke et al. 2010, Johnsen, Leu & Gradinger 2020). The high difference in α (table 3.1) between the USV and UAV sample suggests the lack of pigments and low light availability is the main reason for poor signal of brown algae in the UAV photomosaic.

Brown algae in the UAV photomosaics was only found, sampled and classified in flight line 2 (figure 2.2). The flight line 2 photomosaic is radiometrically corrected with the reflectance standard from flight line 6, at approximately 2.5 m depth. The area covered in flight line 2 is less deep, at an average 1 - 2 m deep. This causes the brown algae to appear brighter, and with an upward tilt in the red light caused by the overestimation of red light attenuation.

Determination of optically shallow nature types within the brown algae pigment class mostly requires trained personnel or salinity measurements. This makes it difficult to differentiate further between the nature types using only the hyperspectral photomosaics. It is however possible to use publicly available depth data to differentiate between M1 Euphotic solid bottoms and M3 solid intertidal bottoms to some extent.

4.2.4 Sediment

As opposed to the other classes, the sediment contain no significant concentration of pigments, hence no distinct lack of reflectance peaks. The R(λ) of sediment sampled from both the USV and the UAV photomosaics are only 3° (table 3.1) different to sediment measured in the spectrometer. It is possible to make out a general shapes in the R(λ) (figure 3.7), which seems to match that of calciferous sediments (Hochberg & Atkinson 2003).

The only conspicuous feature of the R(λ) is a vague trough observed on both the spectrometer and USV sample, which is an absorption peak at 670 nm. The absorption peak is likely caused by a layer of microphytobenthos (Méléder et al. 2018, Hochberg & Atkinson 2003). Microphytobenthos cover the surface of undisturbed marine sediments, and should be expected when imaging any sediment based nature type. The spectrometer samples however were disturbed as they were collected, likely overturning and burying some of the microphytobenthos. Using a sampling method which preserves the upper layer of the sediment (Bouma & Marshall 1964) might improve the similarity between the training data and the photomosaic samples.

Sediment has a higher general reflectance than both seagrass and brown algae (fig-

ures 3.4,3.6). Red algae also has a high general reflectance as they contain coralline structures and are usually closer to the lens. This explains why sediment is generally more comparable to red algae in terms of their high general reflectance. Seeing that the noise intereferrence is much higher in sediment (figure 3.7) than in red algae (figure 3.5), despite both having a high general reflectance, suggests that the main source of noise is related to water attenuation with depth stemming from a lack of available light.

The spectrometer sample in this study contains loose sediment at different grain sizes, a combination of sand, clay and gravel. All three have similar R(λ), but at different light intensities. It is unclear whether bedrock and larger boulders along the Norwegian coast have a similar reflectance, and can be included into the same class.

An interesting angle which arose as a result of this study is the potential for using sediment as a reflectance standard for radiometric correction. Sediment appear to have a relatively flat R(λ) (figure 3.7). This obviously depends on the seasonal cover of microphytobenthos (Méléder et al. 2018) and the composition of the sediment. As sediment is not completely equally reflective, and only reflects about 40% of light, it is inferior to using a white reflectance standard. It should instead be used in cases where a white reflectance standard is not available. This requires further research before utilization.

4.3 SAM classification & accuracy assessment

4.3.1 USV photomosaic classification & accuracy assessment

From the RGB camera mounted within the UHI casing, the *C. filum* in panel b (figure 3.8) was seen brushing across the lens of the UHI as the USV traveled. The close proximity to *C. filum* may have covered several pixels around where the specimen appears in the transect, if only for a brief time, resulting in spectral mixing of affected pixels. This gives a false signature of brown algae leading to its overclassification in panel b (figure 3.8).

SAM classification of the USV photomosaic had a total accuracy of 63.4% (table 3.2). Similar studies have previously assessed the classification accuracy from different platforms under similar circumstances (Mogstad et al. 2019, Rossiter et al. 2020, Freitas et al. 2018) and achieved higher accuracy in classification. Underclassification happened in all four groups, and suggests the calculated α were too small if one wanted to classify the whole seagrass meadow.

The SAM classification of the USV photomosaic has a very low level of false positives, meaning confidence in the classified pixels is very high. An overclas-

sificaiton of seagrass near the deep parts of the transect is expected if there is a high concentration of green algae in the water. IOPs in areas deeper (i.e. the start and end of the transect line) than the reflectance standard are not accounted for during radiometric correction. Seagrass are likely classified in these areas as phytoplankton and seagrass have the same R(λ) peak at 550 nm and 630 nm. This is because chlorophyll *a* and *b*, which occurs in both phylum, has absorbance dips at these wavelengths (Thorhaug et al. 2007). The underclassification of seagrass throughout the transect is owing to the factors mentioned in section 4.2.1. The underclassification of sediment may be caused by the mentioned microphytobenthos of undisturbed sediments having a larger influence on the R(λ) than on the disturbed sediments which were measured in the spectrometer.

4.3.2 UAV photomosaic classification & accuracy assessment

Seagrass and brown algae are severely overclassified (figure 3.9). The sampled R(λ) of both classes looked similar (figures 3.4,3.6), and if calculated may have had a smaller α between them than either sample had to their respective spectrometer R(λ). The classification of seagrass and brown algae appears to cover most pixels from the water column which are not already put to another class, hence both classes seem to better represent the general IOPs, than either of their pigment groups. Classification of red algae and sediment are highly accurate, and suggest the low light availability was not an obstacle to their classification.

The SAM classification of the UAV photomosaic obtained an overall accuracy of only 24.8% (table 3.3). This can be attributed to several previously mentioned factors reducing the overall quality of the UAV photomosaic. Seagrass classification contained a high rate of false positives, as much of the water column was classified as seagrass. Red algae and sediment however, had relatively low levels of false positives, indicating that the confidence in these classifications are very high.

Tait et al. (2019) and James et al. (2020), although using different classifications, and different classification accuracy tests, achieved higher accuracy. Freitas et al. (2018) used a similar setup, comparing SAM to another commonly used classification, and also achieved higher accuracies. This indicates the need for acquiring further experience and knowledge with UAV-HI. The most obvious issues being the aforementioned lack of available light, and the low concentration of photosynthetic pigments. Based on the relative success of the aforementioned studies, and the high accuracy of red algae an sediment classification, UAV-HI mapping of nature types is likely, under the right conditions, a good method for mapping large optically shallow areas despite the low accuracy seen in this study. It is still however only confined to mapping the pigment based classes described in this study.

4.4 Comparison of hyperspectral USV and UAV mapping

This study includes a process of learning by doing as it involved a pioneering multi platform deployment using the USV-UHI and the UAV-HI. For a relevant comparison of the applicability of both methods, one should also take into account the field work and data processing necessary to prepare the data.

The USV-UHI setup weighs approximately 80 kg, had few good holds for carrying, and was deployed on an uneven, long and rocky shore. Deploying the USV demanded three people in waterproof clothing. With expensive sensors reaching deeper than the hull of the boat, there was a constant risk of hitting rocks and shallow seafloor in the study area, which required people to be in the water as precaution. Mission planning and execution in and of itself was performed by one person, with pre-planned routes automatically executed by the vehicle. With improved navigation and georeferencing precision, this gives good repeatability.

A reflectance standard had to be deployed at a significant depth for radiometric correction of the water column in both studies, usually the same depth as the area of interest. This was done by a single person in snorkeling gear.

The UAV took off from the Sletvik field station (NTNU), and was operated by a single pilot. Missions and camera settings were pre-planned, or controlled by the pilot. The UAV obviously had no risk of hitting obstacles in shallow water, and the UAV-HI covers a much larger area per time than the USV-UHI (2460 m^2min^{-1} (UAV mission 2) vs. 30 m^2min^{-1} in this study, figure 1.1). A single transport van was sufficient for each of the platforms as well as their crew and equipment. Both the USV and the UAV can also be deployed from ship. Study areas are therefore only limited by car or boat access, and the platforms spatial range from the host vehicle.

The USV photomosaic in this study was captured in September, and the UAV photomosaic was captured in March. Hence, the difference in signal to noise ratio between the USV and UAV photomosaics should not be a variable upon which these methods are compared and their potential are judged. May and September UAV missions were performed, but resulted in unusable data due to technical issues. Literature consensus suggest there is a "field season" in the summer (Everaerts et al. 2008, Kislik et al. 2018, James et al. 2020), when UAV imaging should be done. This study challenged that notion by utilizing UAV photomosaics captured in March, ultimately finding that UAV missions should in fact be performed in the summer season.

However, while seagrass and brown algae were indistinguishable from each other and from the water column in the UAV photomosaic. The USV photomosaic con-

firmed the existence and position of seagrass, as well as revealing the existence and position of red and brown algae within the seagrass meadow. The use of both photomosaics together allowed for verification of UAV data during post processing, and removed the need for the data analyzer to be knowledgeable about the area.

4.5 Future perspectives

It is clear that the USV is better than the UAV at capturing biological detail and diversity. While the UAV covers much larger geographic areas in the same time, with less risk to equipment. This study should not be seen as a case of which platform is better, as they cover different demands in mapping. The platforms should instead be used in conjunction to provide both large geospatial coverage (by the UAV), and a great level of detail (by the USV).

In further studies, the UAV should cover large areas in preliminary missions, while classifying areas of interest for conservation, management or commercial activity. On the areas of interest, the USV should be deployed to create more detailed maps, or verify the existence and biomass of vulnerable nature types. The detailed information could in turn be used to infer the presence of the same species and a similar biodiversity for similar nature types observed elsewhere from the UAV.

The USV in this study carried a spectral attenuation meter, which provides light attenuation data for depth based radiometric correction of the UAV photomosaics, currently in development. The USV can potentially carry a conductivity, temperature and depth profiler (CTD, Brown & Morrison 1978), or an acoustic current doppler profiler (ADCP, Rowe & Young 1979). Data from these can be added to the UAV photomosaic. Additionally, publicly available wave and current data will enable classification of nature types based on more variables than just the dominant pigment.

Recent publications describe similar methods and their potential for mapping (Freitas et al. 2018, Rossiter et al. 2020, Montes-Herrera et al. 2021). Suggesting that there is currently a shift in which shallow benthic ecological surveys are becoming increasingly more automated. This allows for a repeatable surveys, expanding our understanding of the dynamics controlling nature type and species abundance. The definitive feature of this study is not the amount of data gathered. Instead it is the opportunity to visualize detailed ecological data in a concise way for easier communication, which is the ultimate barrier between scientific discovery and public engagement (Bearzi 2007).

Chapter 5

Conclusion

This study compares the hyperspectral imaging and classification potential of photomosaics from a USV and a UAV. The USV was a good platform for capturing biological detail, but had practical limitations in reach, cover and use. The USV SAM classification reached a high accuracy of 63.4%. The UAV is an efficient platform for large scale mapping, at the cost of pixel size resolution. The UAV photomosaic was captured in March, which is likely why it only reached a SAM classification accuracy of 24.8%.

The UAV-HI mission was performed in March, when the ambient irradiance and pigment content were low, resulting in a low signal to noise ratio. This confirms the existing consensus that UAV missions should be performed in the summer season. It also demonstrates the need for depth dependent radiometric correction, which is in development at the time of writing. This will allow for considerably more accurate classification of pigment based classes, likely down to 10 m depth

The pigment based classes are a reliable classification of nature types, with additional field data allowing for further determination within the nature type system. The pigment based classes may however benefit from a revision by someone with better knowledge of NiN. There could be potential for further

The USV and UAV should be deployed strategically, and in conjunction. Meaning the UAV covers a large area in preliminary survey, classifying areas of interest, while the USV covers areas of interest in greater detail. This will enhance the coverage and detail captured in shallow benthic nature types in future studies, providing detailed and good visualizations for easier communication of Norwegian coastal biodiversity.

Bibliography

Alvsvåg, D. M. (2017), Mapping of a seagrass habitat in hopavågen, sør-trøndelag, with the use of an autonomous surface vehicle combined with optical techniques, Master's thesis, Norwegian University of Science and Technology.

Bearzi, G. (2007), 'Marine conservation on paper', *Conservation Biology* pp. 1–3.

Borowitzka, M. A., Lavery, P. S. & van Keulen, M. (2007), Epiphytes of seagrasses, *in* 'Seagrasses: Biology, Ecology and Conservation', Springer, pp. 441–461.

Bouma, A. H. & Marshall, N. F. (1964), 'A method for obtaining and analysing undisturbed oceanic sediment samples', *Marine Geology* **2**(1-2), 81–99.

Brown, N. & Morrison, G. (1978), Whoi/brown conductivity, temperature, and depth microprofiler., Technical report, Woods Hole Oceanographic institution.

Campbell, J. B. & Wynne, R. H. (2011), History and scope of remote sensing, *in* 'Introduction to remote sensing', 5th edn, Guilford Press, pp. 3–28.

Casazza, G. & Mazzella, L. (2002), 'Photosynthetic pigment composition of marine angiosperms: preliminary characterization of mediterranean seagrasses', *Bulletin of marine science* **71**(3), 1171–1181.

Cohen, J. H., Berge, J., Moline, M. A., Johnsen, G. & Zolich, A. P. (2020), Light in the polar night, *in* 'Polar night marine ecology', Springer, pp. 37–66.

Colombo-Pallotta, M. F., García-Mendoza, E. & Ladah, L. B. (2006), 'Photosynthetic performance, light absorption, and pigment composition of macrocystis pyrifera (laminariales, phaeophyceae) blades from different depths 1', *Journal of Phycology* **42**(6), 1225–1234.

de la Torriente, A., González-Irusta, J. M., Aguilar, R., Fernández-Salas, L. M., Punzón, A. & Serrano, A. (2019), 'Benthic habitat modelling and mapping as a conservation tool for marine protected areas: a seamount in the western mediterranean', *Aquatic Conservation: Marine and Freshwater Ecosystems* **29**(5), 732–750.

De Leeuw, J., Jia, H., Yang, L., Liu, X., Schmidt, K. & Skidmore, A. (2006), 'Comparing accuracy assessments to infer superiority of image classification methods', *International Journal of Remote Sensing* **27**(1), 223–232.

Dekker, A., Brando, V., Anstee, J., Fyfe, S., Malthus, T. & Karpouzli, E. (2007), Remote sensing of seagrass ecosystems: use of spaceborne and airborne sensors, *in* 'Seagrasses: Biology, Ecologyand Conservation', Springer, pp. 347–359.

Erikstad, L., Halvorsen, R. & Simensen, T. (2019), 'Natur i norge (nin) versjon 2.2. inndelingen i landskapstyper', *Artsdatabanken, Trondheim* .

Everaerts, J. et al. (2008), 'The use of unmanned aerial vehicles (uavs) for remote sensing and mapping', *The International Archives of the Photogrammetry, Remote Sensing and Spatial Information Sciences* **37**, 1187–1192.

Fajardo, C. A. B. (2019), Emergency communications network for disaster management, *in* 'Natural Hazards-Risk, Exposure, Response, and Resilience', IntechOpen.

Fearns, P., Klonowski, W., Babcock, R., England, P. & Phillips, J. (2011), 'Shallow water substrate mapping using hyperspectral remote sensing', *Continental Shelf Research* **31**(12), 1249–1259.

Flynn, K. F. & Chapra, S. C. (2014), 'Remote sensing of submerged aquatic vegetation in a shallow non-turbid river using an unmanned aerial vehicle', *Remote Sensing* **6**(12), 12815–12836.

Freitas, S., Almeida, C., Silva, H., Almeida, J. & Silva, E. (2018), *Supervised classification for hyperspectral imaging in UAV maritime target detection*, 2018 IEEE International Conference on Autonomous Robot Systems and Competitions (ICARSC), 18th edn, IEEE.

Fyfe, S. (2003), 'Spatial and temporal variation in spectral reflectance: Are seagrass species spectrally distinct?', *Limnology and Oceanography* **48**(1), 464–479.

Guidetti, P., Lorenti, M., Buia, M. C. & Mazzella, L. (2002), 'Temporal dynamics and biomass partitioning in three adriatic seagrass species: Posidonia oceanica, cymodocea nodosa, zostera marina', *Marine Ecology* **23**(1), 51–67.

Halpern, B. S., Frazier, M., Afflerbach, J., Lowndes, J. S., Micheli, F., O'Hara, C., Scarborough, C. & Selkoe, K. A. (2019), 'Recent pace of change in human impact on the world's ocean', *Scientific reports* **9**(1), 1–8.

Halvorsen, R., Bryn, A. & Erikstad, L. (2015), 'Nin-typeinndeling og beskrivelsessystem for natursystem-nivået', *Natur i Norge, Artikkel* **3**, 1–510.

Heylen, R., Parente, M. & Gader, P. (2014), 'A review of nonlinear hyperspectral unmixing methods', *IEEE Journal of Selected Topics in Applied Earth Observations and Remote Sensing* **7**(6), 1844–1868.

Hochberg, E. J. & Atkinson, M. J. (2003), 'Capabilities of remote sensors to classify coral, algae, and sand as pure and mixed spectra', *Remote Sensing of Environment* **85**(2), 174–189.

Hochberg, E. J., Atkinson, M. J. & Andréfouët, S. (2003), 'Spectral reflectance of coral reef bottom-types worldwide and implications for coral reef remote sensing', *Remote sensing of environment* **85**(2), 159–173.

James, D., Collin, A., Houet, T., Mury, A., Gloria, H. & Le Poulain, N. (2020), 'Towards better mapping of seagrass meadows using uav multispectral and topographic data', *Journal of Coastal Research* **95**(SI), 1117–1121.

Johnsen, G., Leu, E. & Gradinger, R. (2020), Marine micro-and macroalgae in the polar night, *in* 'Polar night marine ecology', Springer, pp. 67–112.

Johnsen, G., Mogstad, A. A., Berge, J. & Cohen, J. H. (2020), Operative habitat mapping and monitoring in the polar night, *in* 'Polar night Marine Ecology', Springer, pp. 277–305.

Johnsen, G., Volent, Z., Dierssen, H., Pettersen, R., Van Ardelan, M., Søreide, F., Fearns, P., Ludvigsen, M. & Moline, M. (2013), Underwater hyperspectral imagery to create biogeochemical maps of seafloor properties, *in* 'Subsea optics and imaging', Elsevier, pp. 508–540e.

Kersen, P., Kotta, J., Bučas, M., Kolesova, N. & Deķere, Z. (2011), 'Epiphytes and associated fauna on the brown alga fucus vesiculosus in the baltic and the north seas in relation to different abiotic and biotic variables', *Marine Ecology* **32**, 87–95.

Kislik, C., Dronova, I. & Kelly, M. (2018), 'Uavs in support of algal bloom research: A review of current applications and future opportunities', *Drones* **2**(4).

Kruse, F. A., Lefkoff, A., Boardman, J., Heidebrecht, K., Shapiro, A., Barloon, P. & Goetz, A. (1993), 'The spectral image processing system (sips)—interactive visualization and analysis of imaging spectrometer data', *Remote sensing of environment* **44**(2-3), 145–163.

Kutser, T., Vahtmäe, E. & Metsamaa, L. (2006), 'Spectral library of macroalgae and benthic substrates in estonian coastal waters', *Proc. Estonian Acad. Sci. Biol. Ecol* **55**(4), 329–340.

Larkum, A. W., Orth, R. J. & Duarte, C. M. (2006), 'Seagrasses: Biology, ecology and conservation', *Phycologia* **45**(5), 5.

Leukart, P. (1994), 'Field and laboratory studies on depth dependence, seasonality and light requirement of growth in three species of crustose coralline algae (corallinales, rhodophyta)', *Phycologia* **33**(4), 281–290.

Lieske, D. J., Wade, T. & Roness, L. A. (2014), 'Climate change awareness and strategies for communicating the risk of coastal flooding: A canadian maritime case example', *Estuarine, Coastal and Shelf Science* **140**, 83–94.

Marshall, M. G. (2021), Annual-Scale (1930-1990) Assessment of Anthropogenic Influences on the Assemblage Structure of Golden-Brown Algae (Chrysophytes) in Crawford Lake, Ontario, Canada, PhD thesis, Carleton University.

Meireles, J. E., Schweiger, A. & Cavender-Bares, J. (2017), 'spectrolab: Class and methods for spectral data in r'. R package version 0.0.16.
URL: *https://CRAN.R-project.org/package=spectrolab*

Méléder, V., Jesus, B., Barnett, A., Barillé, L. & Lavaud, J. (2018), 'Microphytobenthos primary production estimated by hyperspectral reflectance', *PloS one* **13**(5), 1–21.

Mogstad, A. A. & Johnsen, G. (2017), 'Spectral characteristics of coralline algae: a multi-instrumental approach, with emphasis on underwater hyperspectral imaging', *Applied Optics* **56**(36), 9957–9975.

Mogstad, A. A., Johnsen, G. & Ludvigsen, M. (2019), 'Shallow-water habitat mapping using underwater hyperspectral imaging from an unmanned surface vehicle: a pilot study', *Remote Sensing* **11**(6), 685.

Montes-Herrera, J. C., Cimoli, E., Cummings, V., Hill, N., Lucieer, A. & Lucieer, V. (2021), 'Underwater hyperspectral imaging (uhi): a review of systems and applications for proximal seafloor ecosystem studies', *Remote Sensing* **13**(17), 3451.

Moore, K. A. & Short, F. T. (2007), Zostera: biology, ecology, and management, *in* 'Seagrasses: Biology, Ecology and Conservation', Springer, pp. 361–386.

Nababan, B., Mastu, L. O. K., Idris, N. H., Panjaitan, J. P. et al. (2021), 'Shallow-water benthic habitat mapping using drone with object based image analyses', *Remote Sensing* **13**(21), 4452.

Ødegaard, F., Sverdrup-Thygeson, A., Hansen, L. O., Hanssen, O. & Öberg, S. (2009), 'Kartlegging av invertebrater i fem hotspot-habitattyper. nye norske arter og rødlistearter 2004-2008', *NINA Rapport 500* p. 102.

Peirano, A., Damasso, V., Montefalcone, M., Morri, C. & Bianchi, C. N. (2005), 'Effects of climate, invasive species and anthropogenic impacts on the growth of the seagrass posidonia oceanica (l.) delile in liguria (nw mediterranean sea)', *Marine Pollution Bulletin* **50**(8), 817–822.

Ralph, P., Polk, S., Moore, K., Orth, R. & Smith Jr, W. (2002), 'Operation of the xanthophyll cycle in the seagrass zostera marina in response to variable irradiance', *Journal of Experimental Marine Biology and Ecology* **271**(2), 189–207.

Rashmi, S., Addamani, S. & Ravikiran, A. (2014), 'Spectral angle mapper algorithm for remote sensing image classification', *IJISET - International Journal of Innovative Science, Engineering Technology* **1**(4), 201–205.

Rinde, E., Bekkby, T., Kvile, K. Ø., Andersen, G. S., Brkljacic, M. S., Anglès d'Auriac, M., Christie, H. C., Fredriksen, S., Moy, S. R., Staalstrøm, A. et al. (2021), 'Kartlegging av et utvalg marine naturtyper i oslofjorden', *NIVA-rapport* .

Rossiter, T., Furey, T., McCarthy, T. & Stengel, D. B. (2020), 'Uav-mounted hyperspectral mapping of intertidal macroalgae', *Estuarine, Coastal and Shelf Science* **242**, 106789.

Rowe, F. & Young, J. (1979), An ocean current profiler using doppler sonar, *in* 'OCEANS'79', IEEE, pp. 292–297.

RStudio Team (2022), *RStudio: Integrated Development Environment for R*, RStudio, PBC., Boston, MA.
URL: *http://www.rstudio.com/*

Rubasingam, R., Mahmud, M., Gunathilaka, M., Estate, R., Bahru, J. et al. (2011), 'Comparative study between flat and uniform bottom assumptions for snippet imageries in hydrographic applications', *Geoinformation Science Journal* **11**(2), 41–51.

Smith, M. O., Ustin, S. L., Adams, J. B. & Gillespie, A. R. (1990), 'Vegetation in deserts: I. a regional measure of abundance from multispectral images', *Remote sensing of Environment* **31**(1), 1–26.

Smith, R. C. & Baker, K. S. (1978), 'Optical classification of natural waters', *Limnology and Oceanography* **23**(2), 260–267.

Sørensen, A. J., Ludvigsen, M., Norgren, P., Ødegård, Ø. & Cottier, F. (2020), Sensor-carrying platforms, *in* 'Polar night Marine Ecology', Springer, pp. 241–275.

Summers, N., Johnsen, G., Mogstad, A., Løvås, H., Fragoso, G. & Berge, J. (2022), 'Underwater hyperspectral imaging of arctic macroalgal habitats during the polar night using a novel mini-rov-uhi portable system', *Remote Sensing* **14**(6).

Tait, L., Bind, J., Charan-Dixon, H., Hawes, I., Pirker, J. & Schiel, D. (2019), 'Unmanned aerial vehicles (uavs) for monitoring macroalgal biodiversity: comparison of rgb and multispectral imaging sensors for biodiversity assessments', *Remote Sensing* **11**(19), 2332.

Thorhaug, A., Richardson, A. & Berlyn, G. (2007), 'Spectral reflectance of the seagrasses: Thalassia testudinum, halodule wrightii, syringodium filiforme and five marine algae', *International Journal of Remote Sensing* **28**(7), 1487–1501.

Thorne, K., Markharn, B., Barker, P. S. & Biggar, S. (1997), 'Radiometric calibration of landsat', *Photogrammetric Engineering & Remote Sensing* **63**(7), 853–858.

Vahtmäe, E., Kutser, T., Martin, G. & Kotta, J. (2006), 'Feasibility of hyperspectral remote sensing for mapping benthic macroalgal cover in turbid coastal waters—a baltic sea case study', *Remote Sensing of Environment* **101**(3), 342–351.

van Marion, P. (1996), 'Ecological studies in hopavågen, a landlocked bay at agdenes, sør-trøndelag, norway', *Gunneria 71* pp. 1–39.

Ventura, D., Bonifazi, A., Gravina, M. F., Belluscio, A. & Ardizzone, G. (2018), 'Mapping and classification of ecologically sensitive marine habitats using unmanned aerial vehicle (uav) imagery and object-based image analysis (obia)', *Remote Sensing* **10**(9), 1331.

Walday, M. G., Rinde, E., Andersen, G. S., Hancke, K. & Moy, S. R. (2021), 'Frisk oslofjord. undersøkelser på grunt vann-med utprøving av ny teknologi', *NIVA-rapport* .

Wiencke, C., Gómez, I. & Dunton, K. (2010), Phenology and seasonal physiological performance of polar seaweeds, *in* 'Biology of polar benthic algae/Christian Wiencke (ed.) Berlin: de Gruyter', pp. 181–194.

Wolfe, W. L. (1997), *Introduction to imaging spectrometers*, Vol. 25, SPIE Optical Engineering Press, Bellingham, WA, USA.

Yokohama, Y. (1973), 'A comparative study on photosynthesis temperature relationships and their seasonal changes in marine benthic algae', *Internationale Revue der gesamten Hydrobiologie und Hydrographie* **58**(4), 463–472.

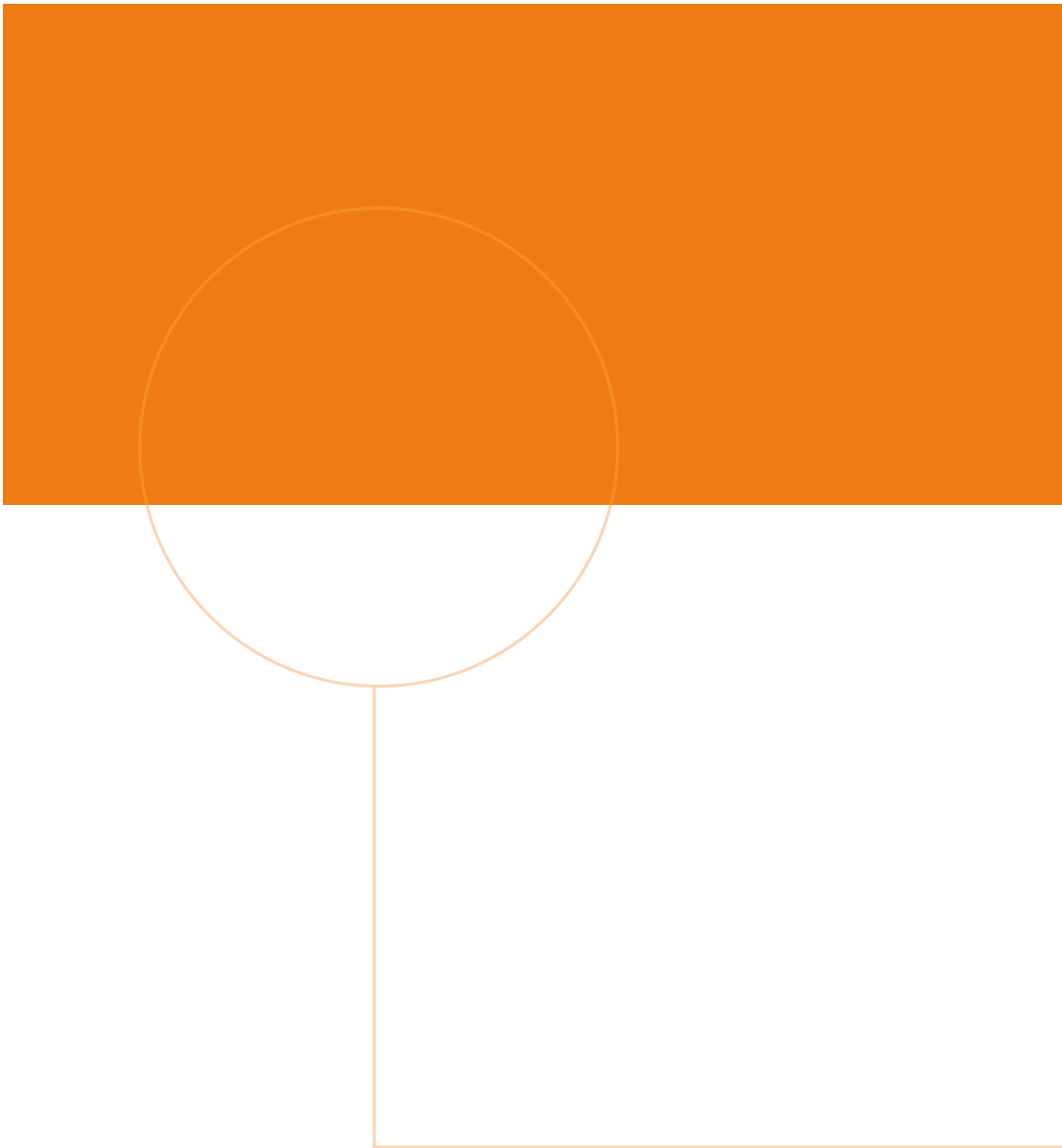

NTNU

Norwegian University of
Science and Technology